Biallelic *TBCD* Mutations Cause Early-Onset Neurodegenerative Encephalopathy

Noriko Miyake,[1,*] Ryoko Fukai,[1,2] Chihiro Ohba,[1,2] Takahiro Chihara,[3] Masayuki Miura,[4,5] Hiroshi Shimizu,[6] Akiyoshi Kakita,[6] Eri Imagawa,[1] Masaaki Shiina,[7] Kazuhiro Ogata,[7] Jiu Okuno-Yuguchi,[8] Noboru Fueki,[9] Yoshifumi Ogiso,[10] Hiroshi Suzumura,[11] Yoshiyuki Watabe,[11] George Imataka,[11] Huey Yin Leong,[12] Aviva Fattal-Valevski,[13] Uri Kramer,[13] Satoko Miyatake,[1] Mitsuhiro Kato,[14] Nobuhiko Okamoto,[15] Yoshinori Sato,[16] Satomi Mitsuhashi,[17,18] Ichizo Nishino,[17,18] Naofumi Kaneko,[19] Akira Nishiyama,[19] Tomohiko Tamura,[19] Takeshi Mizuguchi,[1] Mitsuko Nakashima,[1] Fumiaki Tanaka,[2] Hirotomo Saitsu,[20] and Naomichi Matsumoto[1,*]

We describe four families with affected siblings showing unique clinical features: early-onset (before 1 year of age) progressive diffuse brain atrophy with regression, postnatal microcephaly, postnatal growth retardation, muscle weakness/atrophy, and respiratory failure. By whole-exome sequencing, we identified biallelic *TBCD* mutations in eight affected individuals from the four families. *TBCD* encodes TBCD (tubulin folding co-factor D), which is one of five tubulin-specific chaperones playing a pivotal role in microtubule assembly in all cells. A total of seven mutations were found: five missense mutations, one nonsense, and one splice site mutation resulting in a frameshift. In vitro cell experiments revealed the impaired binding between most mutant TBCD proteins and ARL2, TBCE, and β-tubulin. The in vivo experiments using olfactory projection neurons in *Drosophila melanogaster* indicated that the *TBCD* mutations caused loss of function. The wide range of clinical severity seen in this neurodegenerative encephalopathy may result from the residual function of mutant TBCD proteins. Furthermore, the autopsied brain from one deceased individual showed characteristic neurodegenerative findings: cactus and somatic sprout formations in the residual Purkinje cells in the cerebellum, which are also seen in some diseases associated with mitochondrial impairment. Defects of microtubule formation caused by *TBCD* mutations may underlie the pathomechanism of this neurodegenerative encephalopathy.

Microtubules, cylindrical structures composed of rows of α/β-tubulin heterodimers, are essential components of all eukaryotic cells and are involved in a number of functions such as cell division, morphology, polarization, migration, and intracellular transport.[1,2] Their unique feature of growth (polymerization) and shrinkage (depolymerization) is known as microtubule dynamics.[3,4] α/β-tubulin heterodimers are formed with the aid of tubulin-specific chaperones comprised of five tubulin folding co-factors (TBC): TBCA, TBCB, TBCC, TBCD, and TBCE.[5,6] α- and β-tubulin monomers initially bind with TBCB and TBCA, respectively, and are passed to TBCE and TBCD, respectively, and form complexes together with TBCC and ARL2.[5,7–9]

Of the five TBC genes, only mutations in *TBCE* (GenBank: NM_003193.4; MIM: 604934) have been found to be associated with an autosomal-recessive hypoparathyroidism-retardation-dysmorphism syndrome (MIM: 241410).[10] This is characterized by congenital hypoparathyroidism, microcephaly, hypoplasia of the corpus callosum, intellectual disability, growth failure, and dysmorphic features.[11] It is also associated with a similar disease with bone dysplasia, Kenny-Caffey syndrome (MIM: 244460).[10] Here, we report biallelic mutations in *TBCD* (GenBank: NM_005993.4; MIM: 604649) encoding TBCD and the resulting mutant phenotypes in humans.

In this study, eight affected individuals from two Japanese families, a Chinese family, and an Israeli family were investigated (Figure 1A). The Israeli family was consanguineous, but the others were not. Genomic DNA was extracted from peripheral leukocytes using QuickGene-610L (Fujifilm) or formalin-fixed paraffin-embedded

[1]Department of Human Genetics, Yokohama City University Graduate School of Medicine, Yokohama 236-0004, Japan; [2]Department of Neurology and Stroke Medicine, Yokohama City University Graduate School of Medicine, Yokohama 236-0004, Japan; [3]Department of Biological Science, Graduate School of Science, Hiroshima University, Hiroshima 739-8526, Japan; [4]Department of Genetics, Graduate School of Pharmaceutical Sciences, The University of Tokyo, Tokyo 113-0033, Japan; [5]Agency for Medical Research and Development-Core Research for Evolutional Medical Science and Technology (AMED-CREST), Japan Agency for Medical Research and Development, Tokyo 100-0004, Japan; [6]Department of Pathology, Brain Research Institute, University of Niigata, Niigata 951-8585, Japan; [7]Department of Biochemistry, Yokohama City University Graduate School of Medicine, Yokohama 236-0004, Japan; [8]Department of Neuropediatrics, Nagano Children's Hospital, Azumino 399-8205, Japan; [9]Division of Rehabilitation, Nagano Children's Hospital, Azumino 399-8205, Japan; [10]Department of Clinical Pathology, Nagano Children's Hospital, Azumino 399-8288, Japan; [11]Department of Pediatrics, Dokkyo Medical University School of Medicine, Tochigi 321-0293, Japan; [12]Genetics Department, Hospital Kuala Lumpur, Kuala Lumpur 50586, Malaysia; [13]Pediatric Neurology Unit, Tel Aviv Sourasky Medical Center, Sackler Faculty of Medicine, Tel Aviv University, Tel Aviv 6997801, Israel; [14]Department of Pediatrics, Showa University School of Medicine, Tokyo 142-8666, Japan; [15]Department of Medical Genetics, Osaka Medical Center and Research Institute for Maternal and Child Health, Osaka 594-1101, Japan; [16]Department of Molecular Biology, Yokohama City University Graduate School of Medicine, Yokohama 236-0004, Japan; [17]Department of Neuromuscular Research, National Institute of Neuroscience, National Center of Neurology and Psychiatry, Tokyo 187-8502, Japan; [18]Department of Medical Genome Development, Medical Genome Center, National Center of Neurology and Psychiatry, Tokyo 187-8551, Japan; [19]Department of Immunology, Yokohama City University Graduate School of Medicine, Yokohama 236-0004, Japan; [20]Department of Biochemistry, Hamamatsu University School of Medicine, Hamamatsu 431-3192, Japan

*Correspondence: nmiyake@yokohama-cu.ac.jp (N. Miyake), naomat@yokohama-cu.ac.jp (N. Matsumoto)

http://dx.doi.org/10.1016/j.ajhg.2016.08.005.

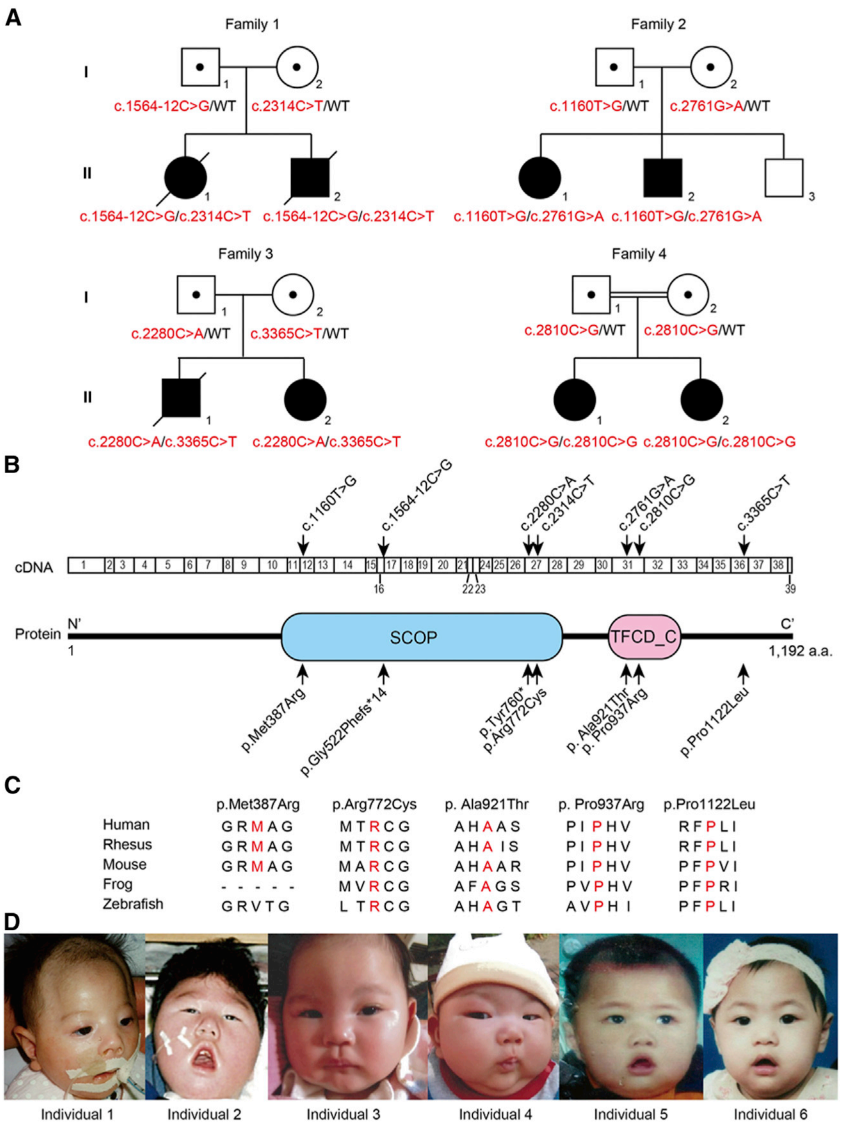

Figure 1. Familial Pedigrees and *TBCD* Mutations

(A) The pedigrees of four families with biallelic *TBCD* mutations. The mutations are shown in red. Affected and unaffected individuals are shown as black and white symbols, respectively. Affected individual identities are as follows: individuals 1 (II-1 in family 1), 2 (II-2 in family 1), 3 (II-1 in family 2), 4 (II-2 in family 2), 5 (II-1 in family 3), 6 (II-2 in family 3), 7 (II-1 in family 4), and 8 (II-2 in family 4).

(B) *TBCD* cDNA and TBCD protein structures. The p.Met387Arg and p.Arg772Cys variants fall within the SCOP domain, and p.Ala921Thr and p.Pro937Arg within the TFCD_C domain. The seven variants found in the cDNA and protein are indicated by arrows. Functional domains of the TBCD protein were predicted by the SMART program.

(C) The evolutionarily conserved amino acids in the missense variants. The conserved amino residues are marked in red.

(D) The facial features of the affected individuals. From left to right, individual 1 at 3 months, individual 2 at 3 years, individual 3 at 4 months, individual 4 at 3 months, individual 5 at 1 year, and individual 6 at 1 year.

brain tissue using QIAamp DNA FFPE tissue kit (QIAGEN) (for individual 1: II-1 in family 1 in Figure 1A) according to the manufacturer's instructions. Blood samples or brain tissue from affected individuals and their families were collected after obtaining written informed consent. The study protocol was approved by the institutional review board of Yokohama City University School of Medicine. To identify the genetic cause of the disease, we performed whole-exome sequencing as described previously.[12] The presence of affected siblings in the families implies an autosomal-recessive mode of inheritance (Figure 1A). Therefore, we focused on genes with homozygous or compound heterozygous variants and identified biallelic *TBCD* mutations in all probands in the four families (Figure 1A and Tables S1–S3). Using Sanger sequencing, we confirmed that the biallelic mutations perfectly co-segregated with the disease status (Figure S1). A total of seven mutations were found in *TBCD*: five missense, one nonsense, and a splicing mutation (Table 1). These variants were unreported or extremely rare (≤ 0.0002) in ExAC, EVS, 1000 Genome, HGVD, and our in-house exome database (n = 575). All of the missense variants were predicted to be pathogenic by PolyPhen-2 and MutationTaster. In addition, four altered amino residues due to missense mutations were located within the functional domains (Figure 1B). Five of the amino residues altered by the missense mutations were evolutionally conserved (four from zebrafish to human and one from mouse to human) (Figure 1C). The intronic mutation (c.1564−12C>G) resulted in an 11-bp insertion of intronic sequence between exons 16 and 17, which was confirmed at the cDNA level to cause a frameshift (p.Gly522Phefs*14) subjected to nonsense-mediated mRNA decay (Figure S2). This genetic evidence strongly indicates that biallelic *TBCD* mutations may cause this neurodegenerative encephalopathy.

The clinical data of all affected individuals are shown in Table 2 and the Supplemental Note. In brief, affected individuals with biallelic *TBCD* mutations showed an early onset of symptoms (before 1 year of age). The first symptoms varied among the families but were similar in affected siblings from the same family: neonatal asphyxia in family 1, decreased movement and hypotonia at 1 month of age in family 2 and at 5 months in family 3, and seizures at 9–11 months in family 4. The affected individuals commonly had progressive clinical courses with muscle weakness, absent visual tracking, and postnatal microcephaly. More than half of the affected individuals had postnatal growth failure, seizure, respiratory failure,

Table 1. Summary of *TBCD* Mutations

Mutation	Amino Acid Change	Position on chr17 (hg19)	dbSNP141	PolyPhen-2 (Score)	MutationTaster (Score)	ExAC	EVS	1000 Genomes	HGVD	In-house (n = 575)
c.1160T>G	p.Met387Arg	80,767,595	no	possibly damaging (0.733)	disease causing (0.996)	no	no	no	no	0
c.1564−12C>G	p. Gly522Phefs*14	80,851,411	no	NA	NA	no	no	no	no	0
c.2280C>A	p.Tyr760*	80,882,834	no	NA	disease causing (1.000)	no	no	no	no	0
c.2314C>T	p.Arg772Cys	80,882,868	rs181969865	probably damaging (0.972)	disease causing (1.000)	no	no	0.0002	no	0
c.2761G>A	p. Ala921Thr	80,887,056	no	probably damaging (1.000)	disease causing (1.000)	no	no	no	no	0
c.2810C>G	p.Pro937Arg	80,887,105	no	probably damaging (1.000)	disease causing (1.000)	no	no	no	no	0
c.3365C>T	p.Pro1122Leu	80,896,008	no	probably damaging (1.000)	disease causing (1.000)	0.00003645	no	no	no	0

The description of the mutation was based on GenBank: NM_005993.4. Abbreviations are as follows: ExAC, Exome Aggregation Consortium; EVS, Exome Variant Server; HGVD, Human Genetic Variation Database; NA, not applicable. Data of minor allele frequencies were examined in May 2016.

regression, optic nerve atrophy, hypotonia, and muscle atrophy. In addition, two affected individuals had variable blood pressure and two other individuals showed urinary incontinence, one of whom also had fecal incontinence, suggesting an involvement of the autonomic system in some affected individuals. Six affected individuals in three of the families became immobile and five required respiratory management. Three of the eight affected individuals were deceased by 20 years of age. Most affected individuals had muscle weakness and atrophy. A muscle biopsy at 12 days of age (corrected gestational age: 5 days) in individual 2 (family 1, II-2) revealed the following myopathic changes: (1) variation in moderate muscle fiber size, ranging from 5 to 15 μm in diameter (Figure 2A); (2) numerous type 2C fibers; (3) atrophy of type 1 muscle fibers (Figure 2B and 2C); and (4) dot-like staining in the myofiber cytoplasm after the NADH-tetrazolium reductase reaction (Figure 2D). The neuromuscular junction was not included in the section. No evidence of neuropathy was observed. These findings may reflect the immaturity of muscle fibers. However, it was not possible to confirm this because only limited samples were available. Interestingly, four affected individuals had episodes of elevated creatine kinase (CK). The elevation of CK was noticed only at birth (individual 1, 1,338 IU/L; individual 2, 1,345 IU/L) in family 1, and at several time points in individual 3 (max. 285 IU/L at 7 months) and individual 4 (max. 752 IU/L at 11 months) (Table 2, Supplemental Note). We believe that elevated CK was caused by asphyxia and bone fracture in family 1 and by frequent episodes of afebrile seizures in family 2. However, the actual triggers remain unclear. Brain imaging studies from three affected individuals indicated progressive brain atrophy involving the cerebrum, corpus callosum, cerebellum, and brain stem (Figures 3 and S3). As early as 3 months of age, atrophy in the frontal lobe and enlarged ventricles (especially in the frontal horn of the lateral ventricles) were detected. Despite the flat and expressionless faces, downturned corners of the mouth, and open mouths, we did not see any specific dysmorphic features (Figures 1D and S4).

Interestingly, some clinical features overlapped between biallelic *TBCD* and *TBCE* mutations: early-onset (<1 year) intellectual disability, postnatal growth failure, hypoplastic corpus callosum, and microcephaly are common in both diseases, while intrauterine growth retardation and hypoparathyroidism were not seen in individuals with *TBCD* mutations (Table S4).[11,13]

TaqMan assays revealed that *TBCD* was ubiquitously expressed in all tissues, but highly expressed in brain, heart, and skeletal muscle in the fetus and adult (Figure S5). The expression pattern was consistent with the affected organs, including the central nervous system and skeletal muscles, in affected individuals with *TBCD* mutations.

An autopsy was performed on individual 1 (family 1, II-1). Although no malformation of the internal organs was detected (Table S5), striated muscle volume, including the iliopsoas, was severely decreased and the diaphragm was extremely thin. The brain and spinal cord were generally atrophic. In the cerebrum, there was severe atrophy of the cortex and white matter and the lateral ventricles were markedly dilated (Figure 2E). The corpus callosum was rudimentary, although the basal ganglia and thalamus were generally well formed. Both the anterior and posterior limbs of the internal capsules were severely atrophic.

Table 2. Genetic and Clinical Information of the Affected Individuals with *TBCD* Mutations

Family ID	Family 1		Family 2		Family 3		Family 4	
Ethnicity	Japanese		Japanese		Chinese		Israel	
Mutations and Variations	c.1564−12C>G (splicing), c.2314C>T (p.Arg772Cys)		c.1160T>G (p.Met387Arg), c.2761G>A (p. Ala921Thr)		c.2280C>A (p.Tyr760*), c.3365C>T (p.Pro1122Leu)		c.2810C>G (p.Pro937Arg), c.2810C>G (p.Pro937Arg)	
Sex	female	male	female	male	male	female	female	female
Individual ID	II-1	II-2	II-1	II-2	II-1	II-2	II-1	II-2
Individual number	individual 1	individual 2	individual 3	individual 4	individual 5	individual 6	individual 7	individual 8
Pregnancy	hydramnion	hydramnion	normal	normal	normal	normal	normal	normal
Age of onset	at birth	at birth	1 month	1 month	5 months	5 months	11 months	9 months
Initial symptom(s)	asphyxia, bone fracture	asphyxia, bone fracture	paucity of movement	hypotonia	hypotonia, regression	hypotonia, regression	febrile seizure	generalized seizure
Age of evaluation	4 years	19 years	9 years	5 years	2 years	3 years	17 years	16 years
Growth failure[a]	yes	yes	yes	yes	yes	yes	no	no
Seizure	no	no	West syndrome	cataplexy	GTS	GTS	GTS/GTCS	GTS/GTCS
Onset age of seizure	ND	ND	4 months	6 months	6 months	1 years	11 months	9 months
Respiratory failure	yes	yes	yes	yes	yes	no	no	no
Regression	ND	ND	yes	yes	yes	yes	yes	yes
Visual tracking	no	no	no	no	no	no	no	no
Optic nerve atrophy	no	yes	yes	yes	yes	no	no	no
Postnatal microcephaly	yes	yes	yes	yes	yes	yes	yes	yes
Ataxia	ND[b]	ND[b]	yes	yes	no	no	no	no
Hypotonia	yes	yes	yes	yes	yes	yes	no	no
Muscle weakness	yes	ND[b]	yes	yes	yes[c]	yes[c]	yes	yes
Muscle atrophy	yes	yes	yes	yes	no	no	yes	yes
Fasciculation[d]	no	no	yes	yes	no	no	no	no
Urinary incontinence	ND	yes[e]	no	no	no	no	yes	no
Fecal incontinence	no	no	no	no	no	no	yes	no

(*Continued on next page*)

Table 2. *Continued*

Family ID	Family 1		Family 2		Family 3		Family 4	
Disturbed sweating	no	no	no	no	no	no	no	no
Blood-pressure variability	ND	no	moderate	moderate	ND	ND	no	no
Elevation of CK	yes	yes	yes	yes	no	no	no	no
Prognosis	immobile with ventilation and deceased at 4 years (respiratory failure)	immobile with ventilation and deceased at 19 years (anaphylactic reaction)	immobile with ventilation	immobile with ventilation	immobile with ventilation and deceased at 4 years (pneumonia)	immobile	walking, moderate intellectual disability	walking, moderate intellectual disability

Abbreviations are as follows: ND, no data; GTS, generalized tonic seizure; GTCS, generalized tonic clonic seizure; CK, creatine kinase.
[a]Judged as height < −2 SD.
[b]Not assessed because individual was immobile.
[c]Floppy and almost immobile.
[d]Fasciculation in tongue.
[e]Neurogenic bladder.

Histopathological examination revealed systemic laminar necrosis in the cerebral cortex, although a normal six-layer structure was observed with no cytologically abnormal neurons, such as dysmorphic neurons or balloon cells (Figure 2F). Furthermore, the hippocampus, thalamus, pontine nucleus (Figure 2G), globus pallidus, and inferior olivary nucleus had severe neuronal loss and gliosis. Many globular structures of unknown origin were observed in the internal segment of the globus pallidus. Purkinje and granule cells in the cerebellum were severely depleted.

These histological abnormalities might be ascribable, at least in part, to intrapartum asphyxia, in which the pattern of neuronal injury may be almost comparable to that of “full-term” severe asphyxia.[14] However, in this individual, other anatomical regions susceptible to asphyxial injury in term infants, including the putamen (Figure 2H), quadrigeminal bodies, substantia nigra (Figure 2I), and dorsal vagal nucleus, had only mild gliosis without apparent neuron loss. Additionally, in the cerebellum, many residual Purkinje cells had focal swellings of the dendrites (cactus/asteroid bodies) (Figure 2J) and some had halo-like amorphous structures around the cell bodies (somatic sprouts) (Figure 2K). Neuronal depletion was severe in the dentate nucleus (Figure 2L). In addition, the brainstem lower motor neuron (LMN) nuclei, including the oculomotor and hypoglossal nuclei, had severe neuronal loss and associated gliosis. In the spinal cord, the lateral corticospinal tracts and dorsal column showed severe degeneration with myelin pallor (Figure 2M). The anterior horns showed severe loss of the LMNs and associated gliosis, which was somewhat more apparent in the lateral nuclear group (Figure 2N). The spinal anterior roots were severely atrophic, whereas the posterior roots were preserved. The diaphragm was severely degenerated with fibrosis and scattered pyknotic nuclear clumps (Figure 2O).

We constructed homology-modeled structures of human TBCD using the Protein Homology/analogY Recognition Engine v.2.0 (Phyre2) server,[15] because no experimental structure is available. The resultant models had α-solenoid repeats with pairs of antiparallel alpha helices, which have a deformable nature. We also employed an in silico detector of an α-solenoid repeat based on an amino acid sequence, Alpha-rod Repeat Detector 2 (ARD2)[16] to verify the modeled structures. The results by ARD2 were consistent with those by the Phyre2 prediction (data not shown).

In the structures obtained, the side chains of Met387 and Ala921 are buried in the hydrophobic cores of α solenoid repeat (Figure S6A). Therefore, the p.Met387Arg and p.Ala921Thr variants might affect the folding of the α-solenoid repeat. The methylene part of the Arg772 side chain is part of a hydrophobic core and the guanidium group is exposed to the protein surface in the modeled structure (Figure S6A). Thus, the p.Arg772Cys variant might also affect at least the folding structure. Because Pro937 and Pro1122 were predicted to reside within a loop between antiparallel α helices and be exposed to a protein surface

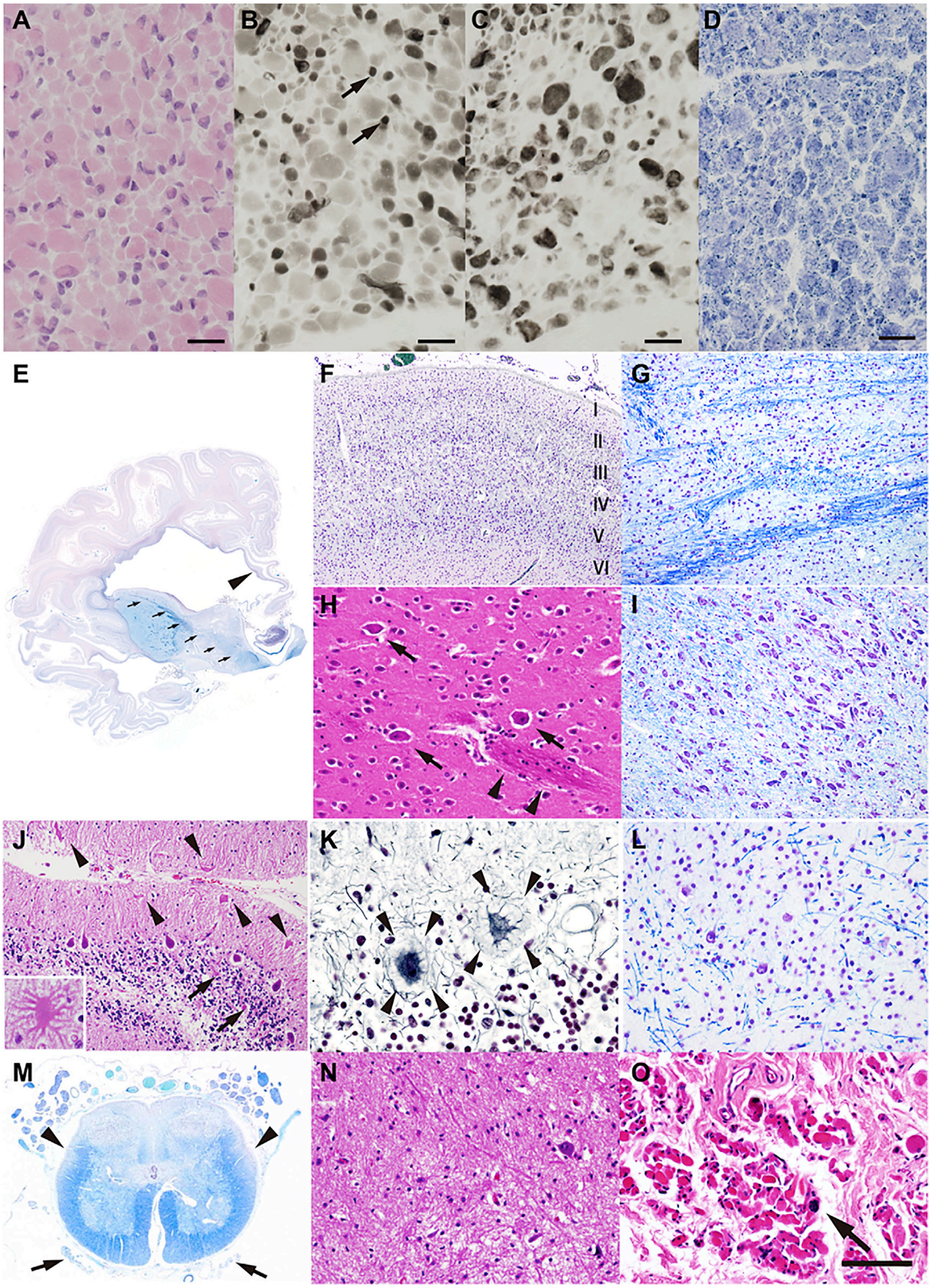

Figure 2. Histopathological Findings in an Individual with Biallelic *TBCD* Mutations

(A–D) Histology of a muscle biopsy from individual 2 at the age of 12 days (corrected gestational age: 5 days). Shown are (A) hematoxylin and eosin staining, (B) myosin ATPase (pH 4.2), (C) myosin ATPase (pH 10.5), and (D) NADH-tetrazolium reductase. The arrows indicate type 1 fibers. Scale bars represent 20 μm.

(E) The cerebral cortex of individual 1 showing systemic laminar necrosis, which is more marked in the temporal lobe. The white matter is also atrophic and associated with marked dilatation of the lateral ventricles. The corpus callosum (arrowhead) and posterior limb of the internal capsule (arrows) are thin. The basal ganglia and thalamus are generally well formed.

(F) The frontal cortex has a normal six-layer architecture. Laminar necrosis is evident in the middle cortical layers.

(legend continued on next page)

(Figure S6A), the p.Pro937Arg and p.Pro1122Leu variants might affect the loop structure and/or interactions with other molecules, although no functional data are available. TBCD functions as a component of the tubulin chaperone multiprotein complex (Figure S6B).[17] Therefore, all of the variants described here have the potential to impair complex formation.

Next, we examined protein-protein interactions between TBCD (wild-type and mutant) and other complex components (α/β-tubulin, TBCE, TBCC, and ARL2) by co-immunoprecipitation. The open reading frames of human *TBCD*, *TBCE*, *TBCC* (GenBank: NM_003192.2), and *ARL2* (GenBank: NM_001667.3) were amplified using human cDNA as a template purchased from Clontech. The PCR products were cloned into the Gateway pDONR221 vector (Life Technologies) to create the entry clones, and each sequence was confirmed by Sanger sequencing. The QuickChange II XL Site-Directed Mutagenesis Kit (Agilent Technologies) was used to create mutant constructs. To create the transient mammalian expression vectors, each entry clone was used for LR recombination with pcDNA3.1/nV5-DEST (for N′ V5-tagged TBCC or TBCE), pcDNA-DEST53 (for N′ GFP-fused TBCD), or pcDNA-DEST40 (for C′ V5-6xHis-tagged ARL2). Wild-type TBCD interact with ARL2, TBCE, and β-tubulin (Figure 4). No apparent binding was observed between TBCD and α-tubulin or TBCD and TBCC (data not shown); therefore, we focused on TBCD binding with ARL2, TBCE, and β-tubulin. As for the binding with ARL2, TBCD mutants p.Met387Arg almost completely, and p.Arg772Cys, p.Ala921Thr, p.Pro1122Leu, and p.Tyr760* partially, lost binding capacity compared with wild-type TBCD. p.Pro937Arg retained its binding capacity (Figure 4A). Mutant TBCD showed similar impaired binding to TBCE (Figure 4B). All TBCD mutants showed decreased binding to endogenous β-tubulin (Figure 4C). These experiments suggest that all the investigated *TBCD* mutations may impair the proper formation of microtubule chaperone complexes.

Finally, to investigate the possible effects of disease-associated *TBCD* mutations in vivo, we took advantage of mosaic analysis with a repressible cell marker (MARCM) in *Drosophila*, which allowed us to analyze gene function in vivo at single-cell resolution.[18] We expressed membrane-tethered GFP (mouse CD8::GFP, mCD8-GFP) to visualize the neuronal morphology of olfactory projection neurons (PNs) in the intact brain (Figure 5).[19,20] The axons of DL1 PNs elongate and form axonal branches at the calyx of the mushroom body and the lateral horn. The dendrites of PNs target a single glomerulus (DL1 glomerulus) in the antennal lobe, the first olfactory center in the *Drosophila* brain (Figures 5A and S7 for wild-type axon and dendrites, respectively). As we have previously reported,[21] PNs homozygous for *tbcd^1* mutations (*tbcd^1* PNs), in an otherwise largely heterozygous animal, had shorter axons and/or reduced axonal branches (Figures 5B–5D). Next, we carried out a MARCM-rescue experiment, in which we cell autonomously expressed cDNA of wild-type human *TBCD* in *tbcd^1* PNs and found that overexpression of human TBCD significantly suppressed the axonal phenotypes of *tbcd^1* PNs (Figure 5E). In addition, the dendritic phenotype of *tbcd^1* PNs also tended to be suppressed by human *TBCD* overexpression (Figure S7). These results suggest that the function of TBCD in neuronal morphogenesis is partly conserved between *Drosophila* and humans.

To test the effect of disease-associated *TBCD* mutations, we performed MARCM-rescue experiments with human *TBCD* carrying disease-associated mutations. To avoid the positional effect that causes unexpected transgene expression differences, we utilized the PhiC31-integrase system to generate *UAS* transgenic animals and all the *UAS* transgenes were inserted in an *attP2* landing site.[22] Human *TBCD* bearing a disease-associated mutation was less able to suppress the axonal phenotype of *tbcd^1* PN compared with wild-type human *TBCD* (Figure 5E). A similar tendency was also observed in PN dendrites (Figure S7). These results indicate that the *TBCD* disease-associated mutations we tested cause loss of function of the TBCD protein.

In this study, we have reported four families with early-onset neurodegenerative encephalopathy associated with biallelic *TBCD* mutations. Core clinical features include early-onset progressive diffuse brain atrophy with regression, postnatal microcephaly, postnatal growth delay, muscle weakness/atrophy, and respiratory failure. Our in vitro and in vivo studies showed that seven *TBCD* mutations are likely to lead to loss of function of the TBCD protein. Interestingly, the clinical course was very similar

---

(G) The pontine nucleus with severe neuronal loss and gliosis. Note that both the longitudinal and transverse fibers are degenerative, and longitudinal fibers are almost unrecognizable.

(H) The putamen has a normal composition of medium spiny and large aspiny neurons (arrows). The putamino-pallidal fibers are evident (arrowheads).

(I) Substantia nigra is well preserved in this individual.

(J–L) Loss of Purkinje and granule cells is evident in the cerebellum. The residual Purkinje cells show torpedoes (J, arrows) and asteroid bodies/cactus (J, arrowheads and inset), as well as halo-like amorphous structures (somatic sprouts) (K, arrowheads). Neuron loss is also apparent in the dentate nucleus (L).

(M) Anterior horn volume is reduced in the lumbar cord. The anterior nerve roots are severely atrophic (arrows), whereas the posterior roots are almost preserved. Degeneration of the lateral corticospinal tracts (arrowheads) and posterior column is also evident.

(N) The lumbar anterior horn with severe loss of the lower motor neurons and associated gliosis.

(O) Severe degeneration of the muscle fibers in the diaphragm, with fibrosis and scattered pyknotic nuclear clumps (arrow).

Shown are Klüver-Barrera staining (E, F, G, I, L, M), hematoxylin and eosin staining (H, J, N, O), and Bodian staining (K). Scale bars represent 1 cm (E), 500 μm (F), 200 μm (G, I), 100 μm (H, L, N, O), 160 μm (J), 50 μm (J inset and K), and 1.5 mm (M).

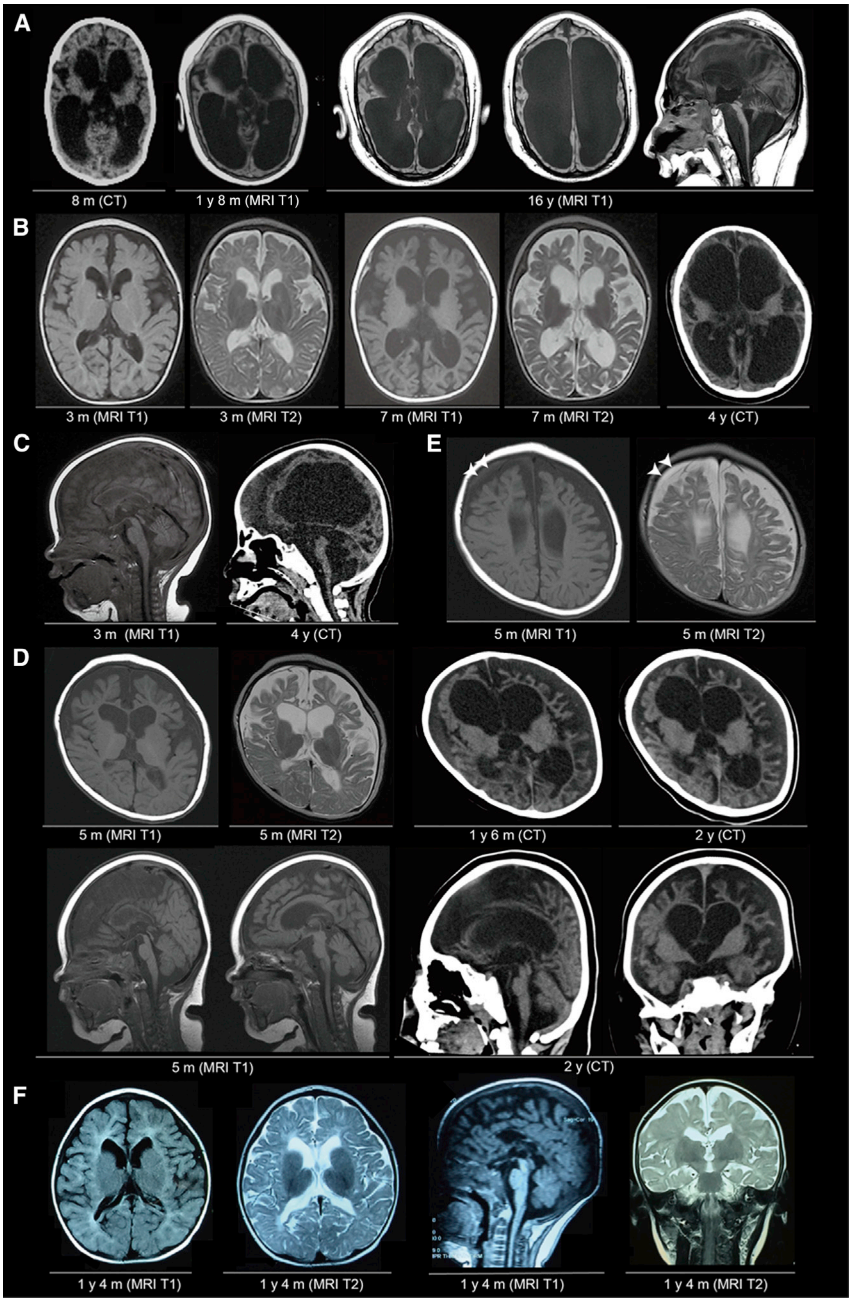

Figure 3. Neuroimaging of Affected Individuals with Biallelic *TBCD* Mutations

(A) The neuroimages of individual 2 at 8 months (computed tomography: CT), 1 year 8 months and 16 years (T1-weighted MRI). Severe, progressive enlargement of bilateral ventricles, thin brain stems, and severe cerebellar atrophy are shown.

(B) The axial brain paired T1- and T2-weighted MRI images of individual 3 at 3 months and 7 months and CT at 4 years (right).

(C) The sagittal images of individual 3. T1-weighted MRI at 3 months (left) and CT at 4 years (right). Thinned corpus callosum and enlargement of the great cistern can be seen on the MRI (left).

(D) The serial images from individual 4. From upper left to upper right, axial T1-weighted MRI and T2-weighted MRI at 5 months, CT at 1 year 6 months, and CT at 2 years. Gyral pattern and myelination seemed to be consistent with age, whereas the progressive atrophy of the cerebral cortex (predominantly in the frontal cortex) and enlargement of the ventricles is remarkable. From lower left to lower right, two sections of sagittal T1-weighted MRI at 5 months, sagittal and coronal sections from CT at 2 years.

(E) T1- and T2-weighted MRI images of individual 4 at 5 months. The white arrowheads indicate a chronic subdural hematoma.

(F) T1- and T2-weighted MRI images of individual 6 at 1 year 4 months.

within individual families, but differed between families. This might be partly explained by the specific mutations in each family. The siblings in family 4 with a homozygous missense mutation (c.2810C>G [p.Pro937Arg]) had a milder phenotype, possibly because binding of the altered TBCD protein with β-tubulin was only mildly affected. In more severe clinical cases (such as the deceased individuals in families 1 and 3), affected individuals carried truncating and missense variants that significantly impaired TBCD binding to ARL2, TBCE, and β-tubulin (Table S6). This indicates that biallelic *TBCD* mutations may lead to a wide range of clinical severities depending on the level of residual protein function resulting from the specific *TBCD* mutation.

We neuropathologically examined an autopsied individual (individual 1) in whom the original lesions caused by *TBCD* mutations could have been masked by asphyxial effects. However, we found the following pathological findings that could not be easily explained by asphyxia: (1) neuronal loss of dentate nuclei of the cerebellum and LMN in the brainstem and anterior horn of the spinal code and (2) somatic sprout and cactus formations in cerebellar Purkinje cells. Neuronal loss in the dentate nuclei and LMN may also be caused by asphyxia.[23] However, regions that are known to be susceptible to asphyxia, such as the putamen and quadrigeminal bodies,[14] were well preserved in this affected individual. Therefore, the disproportionally severe loss of LMNs in the brainstem, spinal cord, and the cerebellar dentate nucleus may arise from lesions caused by *TBCD* mutations, rather than asphyxia. In addition, cactus formations are usually observed in Menkes disease and mitochondrial diseases,[24–26] and somatic sprouts have been reported in Menkes disease and spinocerebellar ataxia type 31,[27–29] but not in asphyxia. Notably, mitochondrial dysfunction is also associated with Menkes disease.[30]

Mitochondria are essential organelles providing energy to all eukaryotic cells. Most mitochondria are newly produced in the soma and are transported to the distal end of axons and dendrites.[31–33] In neurons, mitochondria are distributed unevenly through microtubule trafficking, depending on local energy demand.[33–36] Microtubules are essential for long-distance axonal transport,[32,37] and impaired mitochondrial transport results in neuronal degeneration.[33,38–40] Reduced levels of TBCD protein affect microtubule network formation and impair microtubule transport in *tbcd*^{1} PNs.[41] Furthermore, TBCD is also required for axon and dendrite maintenance in PNs.[41] Therefore, TBCD depletion may result in an abnormal microtubule network and abnormal microtubule trafficking in the human brain. Consequently, energy supply to neuronal cells is reduced, causing neuronal degradation. The formation of cactus and somatic sprouts might reflect structural and metabolic abnormalities resulting from disrupted mitochondrial transport in neuronal cells caused by TBCD depletion.

In conclusion, we have described an early-onset neurodegenerative encephalopathy caused by biallelic *TBCD* mutations. We performed in vitro and in vivo experiments which revealed that the described *TBCD* mutations probably cause loss of function of the TBCD protein. We also investigated a possible genotype-phenotype correlation, particularly with regard to disease severity. Our knowledge of human *TBCD* mutations is currently limited, and therefore more genetic and clinical studies are required to better understand the clinical consequences of *TBCD* mutations.

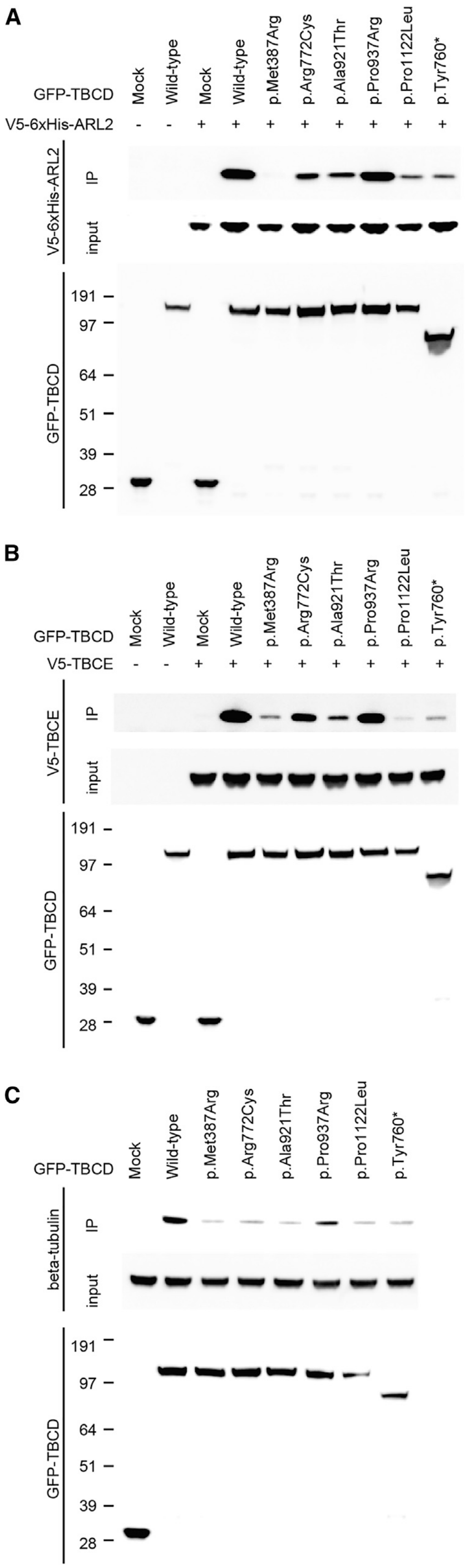

Figure 4. Intermolecular Associations between TBCD and Its Binding Partners

(A and B) The molecular interaction between human TBCD and ARL2 (A) or TBCE (B). GFP-fused wild-type TBCD (159 kDa) or its mutants were transiently co-overexpressed with V5-6xHis-tagged ARL2 (22 kDa) or V5-tagged TBCE (60 kDa) in HEK293T cells using the X-treme GENE9 DNA transfection kit (Roche). At 48 hr after transfection, the cells were collected and lysed with lysis buffer (25 mM Tris-HCl [pH 7.5], 100 mM NaCl, 2 mM EDTA, 0.5% Triton X-100, and protease inhibitors). GFP-fused TBCD proteins were immunoprecipitated using a rabbit polyclonal anti-GFP antibody (Abcam cat# ab6556, RRID: AB_305564) and Dynabeads Protein-G (Thermo Fisher Scientific). Input and immunoprecipitated samples (IP) were immunoblotted with mouse monoclonal anti-GFP (Roche) and anti-V5 antibodies (Thermo Fisher Scientific cat# R960-25, RRID: AB_2556564).

(C) The binding of human TBCD and endogenous β-tubulin (50 kDa). Wild-type GFP-fused TBCD or its mutants were transiently overexpressed in HEK293T cells. GFP-fused TBCD proteins were immunoprecipitated with a rabbit polyclonal anti-GFP antibody and immunoblotted with mouse monoclonal anti-GFP or anti β-tubulin antibodies (Chemicon International cat# MAB3408). Horseradish peroxidase-conjugated goat anti-mouse IgG antibody (Jackson ImmunoResearch) was used as the secondary antibody. Immunodetection was performed using Supersignal West Dura Extended Duration Substrate (Thermo Fisher Scientific) on a ChemiDoc Touch Imaging system (Bio-Rad Laboratories).

At least three independent experiments were performed to confirm the consistency of results for TBCD binding with ARL2, TBCE, or β-tubulin. Mock indicates only GFP protein (27 kDa). "+" and "−" denote the presence and absence of V5-tagged proteins (or only V5-tag with the size of 1 kDa, which could not be detected due to its small molecular weight), respectively.

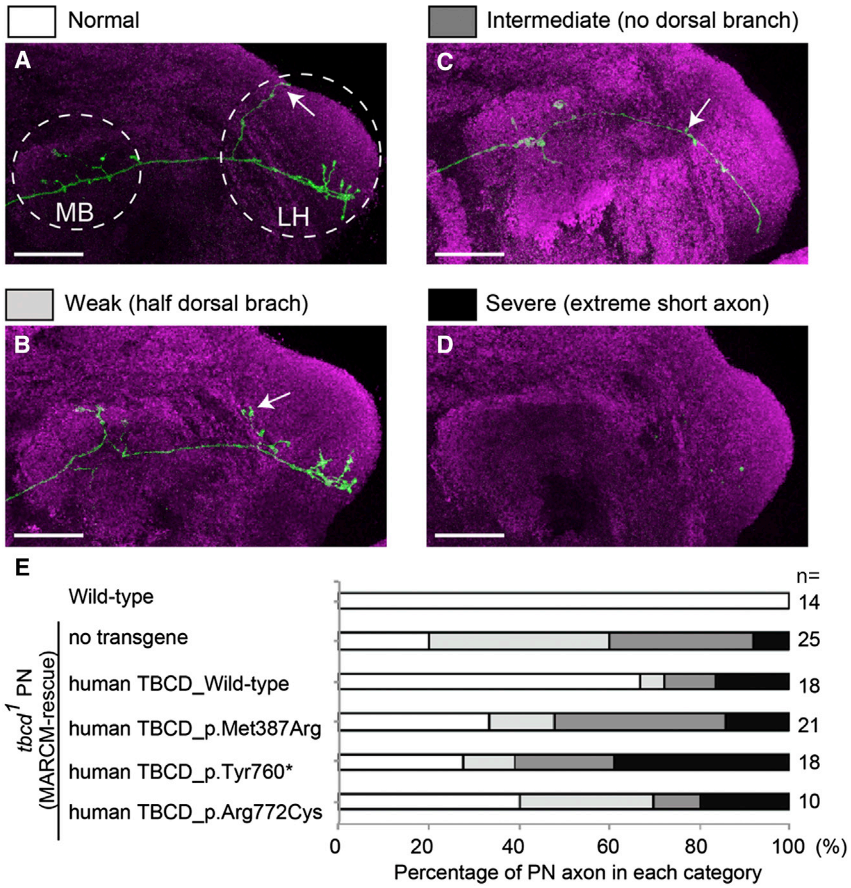

Figure 5. Human *TBCD* with Disease-Associated Mutations Impaired Neuronal Morphology

(A–D) The representative axonal morphologies of *Drosophila* olfactory projection neurons. The axons of DL1 single-cell clones for wild-type *Drosophila* (A) show the typical branching pattern at the calyx of the mushroom body (MB) and lateral horn (LH). Axons of $tbcd^1$ *Drosophila* PNs show branching and elongation defects (B–D). The dorsal branch at the LH is often affected (arrow in A–C). Axons cannot reach the MB in the severe class (no axon is visible in D). PN morphologies and Bruchpilot (presynaptic marker) are shown in green (anti-CD8 antibody) and magenta (nc82), respectively. Scale bars represent 25 μm.

(E) Quantification of MARCM-rescue experiments. Each gray scale corresponds to the colors in (A)–(D) above. n indicates the number of MARCM clones examined. Because the number of clones we can observe in the *Drosophila* brain cannot be controlled, we analyzed a variable number of clones (minimum n = 10). Details for the generation of transgenic flies, MARCM clone induction, immunohistochemistry of fly brains, image processing, and quantification methods are available upon request.

Supplemental Data

Supplemental Data include supplemental note, seven figures, and six tables and can be found with this article online at http://dx.doi.org/10.1016/j.ajhg.2016.08.005.

Acknowledgments

The authors appreciate the participation of all the affected individuals and their families in this study. This work was supported by grants for Research on Measures for Intractable Diseases; Comprehensive Research on Disability Health and Welfare, the Strategic Research Program for Brain Science; Initiative on Rare and Undiagnosed Diseases in Pediatrics and Initiative on Rare and Undiagnosed Diseases for Adults from the Japan Agency for Medical Research and Development; Grants-in-Aid for Scientific Research on Innovative Areas (Transcription Cycle and Comprehensive Brain Science Network) from the Ministry of Education, Science, Sports and Culture of Japan; Grants-in-Aid for Scientific Research (B and C) and Challenging Exploratory Research from the Japan Society for the Promotion of Science; Creation of Innovation Centers for Advanced Interdisciplinary Research Areas Program in the Project for Developing Innovation Systems from the Japan Science and Technology Agency; the Takeda Science Foundation; the Yokohama Foundation for Advancement of Medical Science; and the Hayashi Memorial Foundation for Female Natural Scientists.

Received: May 16, 2016
Accepted: August 9, 2016
Published: September 22, 2016

Web Resources

ExAC Browser (accessed May 2016), http://exac.broadinstitute.org/
GATK, https://www.broadinstitute.org/gatk/
GenBank, http://www.ncbi.nlm.nih.gov/genbank/
Human Genetic Variation Database (HGVD), http://www.genome.med.kyoto-u.ac.jp/SnpDB/
NHLBI Exome Sequencing Project (ESP) Exome Variant Server, http://evs.gs.washington.edu/EVS/
Novoalign, http://www.novocraft.com/main/page.php?s=novoalign
OMIM, http://www.omim.org/
Picard, http://broadinstitute.github.io/picard/
RRID, https://scicrunch.org/resources
SMART, http://www.smart.embl-heidelberg.de/

References

1. Nogales, E. (2001). Structural insight into microtubule function. Annu. Rev. Biophys. Biomol. Struct. *30*, 397–420.
2. Ohi, R., and Zanic, M. (2016). Ahead of the curve: new insights into microtubule dynamics. F1000Res. *5*.
3. Mitchison, T., and Kirschner, M. (1984). Dynamic instability of microtubule growth. Nature *312*, 237–242.
4. Desai, A., and Mitchison, T.J. (1997). Microtubule polymerization dynamics. Annu. Rev. Cell Dev. Biol. *13*, 83–117.
5. Tian, G., Lewis, S.A., Feierbach, B., Stearns, T., Rommelaere, H., Ampe, C., and Cowan, N.J. (1997). Tubulin subunits exist in an activated conformational state generated and maintained by protein cofactors. J. Cell Biol. *138*, 821–832.

6. Lewis, S.A., Tian, G., and Cowan, N.J. (1997). The alpha- and beta-tubulin folding pathways. Trends Cell Biol. *7*, 479–484.
7. Bhamidipati, A., Lewis, S.A., and Cowan, N.J. (2000). ADP ribosylation factor-like protein 2 (Arl2) regulates the interaction of tubulin-folding cofactor D with native tubulin. J. Cell Biol. *149*, 1087–1096.
8. Tian, G., Bhamidipati, A., Cowan, N.J., and Lewis, S.A. (1999). Tubulin folding cofactors as GTPase-activating proteins. GTP hydrolysis and the assembly of the alpha/beta-tubulin heterodimer. J. Biol. Chem. *274*, 24054–24058.
9. Nithianantham, S., Le, S., Seto, E., Jia, W., Leary, J., Corbett, K.D., Moore, J.K., and Al-Bassam, J. (2015). Tubulin cofactors and Arl2 are cage-like chaperones that regulate the soluble αβ-tubulin pool for microtubule dynamics. eLife *4*.
10. Parvari, R., Hershkovitz, E., Grossman, N., Gorodischer, R., Loeys, B., Zecic, A., Mortier, G., Gregory, S., Sharony, R., Kambouris, M., et al.; HRD/Autosomal Recessive Kenny-Caffey Syndrome Consortium (2002). Mutation of TBCE causes hypoparathyroidism-retardation-dysmorphism and autosomal recessive Kenny-Caffey syndrome. Nat. Genet. *32*, 448–452.
11. Sanjad, S.A., Sakati, N.A., Abu-Osba, Y.K., Kaddoura, R., and Milner, R.D. (1991). A new syndrome of congenital hypoparathyroidism, severe growth failure, and dysmorphic features. Arch. Dis. Child. *66*, 193–196.
12. Miyake, N., Tsukaguchi, H., Koshimizu, E., Shono, A., Matsunaga, S., Shiina, M., Mimura, Y., Imamura, S., Hirose, T., Okudela, K., et al. (2015). Biallelic mutations in nuclear pore complex subunit NUP107 cause early-childhood-onset steroid-resistant nephrotic syndrome. Am. J. Hum. Genet. *97*, 555–566.
13. Padidela, R., Kelberman, D., Press, M., Al-Khawari, M., Hindmarsh, P.C., and Dattani, M.T. (2009). Mutation in the TBCE gene is associated with hypoparathyroidism-retardation-dysmorphism syndrome featuring pituitary hormone deficiencies and hypoplasia of the anterior pituitary and the corpus callosum. J. Clin. Endocrinol. Metab. *94*, 2686–2691.
14. Volpe, J.J. (2008). Hypoxic-ischemic encephalopathy. In Neurology of the Newborn, J.J. Volpe, ed. (Philadelphia: Saunders/Elsevier), pp. 347–399.
15. Kelley, L.A., Mezulis, S., Yates, C.M., Wass, M.N., and Sternberg, M.J. (2015). The Phyre2 web portal for protein modeling, prediction and analysis. Nat. Protoc. *10*, 845–858.
16. Fournier, D., Palidwor, G.A., Shcherbinin, S., Szengel, A., Schaefer, M.H., Perez-Iratxeta, C., and Andrade-Navarro, M.A. (2013). Functional and genomic analyses of alpha-solenoid proteins. PLoS ONE *8*, e79894.
17. Tian, G., and Cowan, N.J. (2013). Tubulin-specific chaperones: components of a molecular machine that assembles the α/β heterodimer. Methods Cell Biol. *115*, 155–171.
18. Lee, T., and Luo, L. (1999). Mosaic analysis with a repressible cell marker for studies of gene function in neuronal morphogenesis. Neuron *22*, 451–461.
19. Jefferis, G.S., and Hummel, T. (2006). Wiring specificity in the olfactory system. Semin. Cell Dev. Biol. *17*, 50–65.
20. Sakuma, C., Anzo, M., Miura, M., and Chihara, T. (2014). Development of olfactory projection neuron dendrites that contribute to wiring specificity of the *Drosophila* olfactory circuit. Genes Genet. Syst. *89*, 17–26.
21. Sakuma, C., Okumura, M., Umehara, T., Miura, M., and Chihara, T. (2015). A STRIPAK component Strip regulates neuronal morphogenesis by affecting microtubule stability. Sci. Rep. *5*, 17769.
22. Groth, A.C., Fish, M., Nusse, R., and Calos, M.P. (2004). Construction of transgenic *Drosophila* by using the site-specific integrase from phage phiC31. Genetics *166*, 1775–1782.
23. Clancy, R.R., Sladky, J.T., and Rorke, L.B. (1989). Hypoxic-ischemic spinal cord injury following perinatal asphyxia. Ann. Neurol. *25*, 185–189.
24. Okeda, R., Gei, S., Chen, I., Okaniwa, M., Shinomiya, M., and Matsubara, O. (1991). Menkes' kinky hair disease: morphological and immunohistochemical comparison of two autopsied patients. Acta Neuropathol. *81*, 450–457.
25. Tanahashi, C., Nakayama, A., Yoshida, M., Ito, M., Mori, N., and Hashizume, Y. (2000). MELAS with the mitochondrial DNA 3243 point mutation: a neuropathological study. Acta Neuropathol. *99*, 31–38.
26. Mori, O., Yamazaki, M., Ohaki, Y., Arai, Y., Oguro, T., Shimizu, H., and Asano, G. (2000). Mitochondrial encephalomyopathy with lactic acidosis and stroke like episodes (MELAS) with prominent degeneration of the intestinal wall and cactus-like cerebellar pathology. Acta Neuropathol. *100*, 712–717.
27. Hirano, A., Llena, J.F., French, J.H., and Ghatak, N.R. (1977). Fine structure of the cerebellar cortex in Menkes Kinky-hair disease. X-chromosome-linked copper malabsorption. Arch. Neurol. *34*, 52–56.
28. Sato, N., Amino, T., Kobayashi, K., Asakawa, S., Ishiguro, T., Tsunemi, T., Takahashi, M., Matsuura, T., Flanigan, K.M., Iwasaki, S., et al. (2009). Spinocerebellar ataxia type 31 is associated with "inserted" penta-nucleotide repeats containing (TGGAA)n. Am. J. Hum. Genet. *85*, 544–557.
29. Owada, K., Ishikawa, K., Toru, S., Ishida, G., Gomyoda, M., Tao, O., Noguchi, Y., Kitamura, K., Kondo, I., Noguchi, E., et al. (2005). A clinical, genetic, and neuropathologic study in a family with 16q-linked ADCA type III. Neurology *65*, 629–632.
30. Rossi, L., Lombardo, M.F., Ciriolo, M.R., and Rotilio, G. (2004). Mitochondrial dysfunction in neurodegenerative diseases associated with copper imbalance. Neurochem. Res. *29*, 493–504.
31. Davis, A.F., and Clayton, D.A. (1996). In situ localization of mitochondrial DNA replication in intact mammalian cells. J. Cell Biol. *135*, 883–893.
32. Hollenbeck, P.J. (1996). The pattern and mechanism of mitochondrial transport in axons. Front. Biosci. *1*, d91–d102.
33. Sheng, Z.H., and Cai, Q. (2012). Mitochondrial transport in neurons: impact on synaptic homeostasis and neurodegeneration. Nat. Rev. Neurosci. *13*, 77–93.
34. Li, Z., Okamoto, K., Hayashi, Y., and Sheng, M. (2004). The importance of dendritic mitochondria in the morphogenesis and plasticity of spines and synapses. Cell *119*, 873–887.
35. Ruthel, G., and Hollenbeck, P.J. (2003). Response of mitochondrial traffic to axon determination and differential branch growth. J. Neurosci. *23*, 8618–8624.
36. Hollenbeck, P.J., and Saxton, W.M. (2005). The axonal transport of mitochondria. J. Cell Sci. *118*, 5411–5419.
37. Grafstein, B., and Forman, D.S. (1980). Intracellular transport in neurons. Physiol. Rev. *60*, 1167–1283.

38. Devine, M.J., Birsa, N., and Kittler, J.T. (2016). Miro sculpts mitochondrial dynamics in neuronal health and disease. Neurobiol. Dis. *90*, 27–34.

39. Coleman, M. (2005). Axon degeneration mechanisms: commonality amid diversity. Nat. Rev. Neurosci. *6*, 889–898.

40. Lin, M.Y., and Sheng, Z.H. (2015). Regulation of mitochondrial transport in neurons. Exp. Cell Res. *334*, 35–44.

41. Okumura, M., Sakuma, C., Miura, M., and Chihara, T. (2015). Linking cell surface receptors to microtubules: tubulin folding cofactor D mediates Dscam functions during neuronal morphogenesis. J. Neurosci. *35*, 1979–1990.

The American Journal of Human Genetics, Volume *99*

Supplemental Data

Biallelic *TBCD* Mutations Cause Early-Onset Neurodegenerative Encephalopathy

Noriko Miyake, Ryoko Fukai, Chihiro Ohba, Takahiro Chihara, Masayuki Miura, Hiroshi Shimizu, Akiyoshi Kakita, Eri Imagawa, Masaaki Shiina, Kazuhiro Ogata, Jiu Okuno-Yuguchi, Noboru Fueki, Yoshifumi Ogiso, Hiroshi Suzumura, Yoshiyuki Watabe, George Imataka, Huey Yin Leong, Aviva Fattal-Valevski, Uri Kramer, Satoko Miyatake, Mitsuhiro Kato, Nobuhiko Okamoto, Yoshinori Sato, Satomi Mitsuhashi, Ichizo Nishino, Naofumi Kaneko, Akira Nishiyama, Tomohiko Tamura, Takeshi Mizuguchi, Mitsuko Nakashima, Fumiaki Tanaka, Hirotomo Saitsu, and Naomichi Matsumoto

Supplemental Note: Case Reports

Family 1

Two affected individuals were born to non-consanguineous Japanese parents. Individual 1 (II-1) was born at 42 gestational weeks by vaginal delivery. Her birth weight was 2864 g [−0.68 standard deviation (SD)]. Mild hydramnion was noted during the pregnancy. Apgar scores were 1 after 1 min and 2 after 5 min. No spontaneous breathing or voluntary movements, even of the face, were observed at birth; therefore resuscitation, intubation, and mechanical ventilation were immediately started. At birth, a weak light reflex, anisocoria (right > left), marked hypotonia, paralysis of the body below the neck, and the absence of deep tendon reflex (DTR) were observed. Bone fractures of the bilateral humerus and left femur, general osteopenia, bowing of the femur and radius, and narrowing of the ribs were also noted. Serum creatine kinase (CK) was elevated at birth (1338 IU/L, normal range: 35–160 IU/L). At 1 month, the light reflex was absent. Brain computed tomography (CT) at 8 months of age showed diffuse atrophy of the cerebrum, cerebellum, brain stem, and cervical cord. Brain magnetic resonance imaging (MRI) at 2 years showed severe diffuse atrophy of the entire central nervous system (CNS) including the spinal cord. Particularly in the cerebellum, normal anatomical structure was almost absent. Muscle CT and MRI did not detect any substantial muscle volume, only soft tissue signals. Facial photographs at 3 months, and 1 year, and 3 years are shown in Figure 1D and Figure S4.

Unfortunately, brain imaging data from this individual were unavailable. Despite a tracheotomy she died of respiratory failure at 4 years of age, and an autopsy was performed.

Individual 2 (II-2) was born at 39 weeks of gestation with Apgar scores of 1 after 1 min and 4 after 5 min. His birth weight, length, and head circumference (HC) were 2867 g (−0.7 SD), 48 cm (−0.63 SD) and 34.5 cm (+0.76 SD). Like Individual 1, no spontaneous breathing or voluntary movements, even of the face, were seen following birth. Severe hypotonia in the extremities, multiple arthrogryposis, and absence of DTR were noted. Serum CK was also elevated at birth (CK 640 IU/L with CK-MB 145 IU/L) and reached maximum CK (1345 IU/L with CK-MB 24 IU/L) at 1 day after birth, and then decreased to the normal range in 6 days (56 IU/L). A muscle biopsy at 12 days after birth revealed nonspecific myopathic changes. Mechanical ventilation was started immediately after birth and a tracheotomy was performed. Neurogenic bladder and swallowing disturbances were also noted. Brain CT at 8 months and 20 months of age showed severe cerebral atrophy and mild atrophy of medulla and midbrain (Figure 3A). Serum and urine amino acid analysis, very long chain fatty acid and urine organic acid analysis, and cerebrospinal fluid examination were all normal. This individual was unresponsive to visual evoked potential and auditory brainstem stimulation. Motor nerve conduction velocity (MCV) and sensory conduction velocity (SCV) could not be measured due to a lack of muscle potential. At 16 years of age, a brain MRI showed progressive severe atrophy of the CNS including the brain stem (Figure 3A). At 19 years of age, his body weight, length, and HC were 150 cm (−3.97 SD), 33.0 kg (−3.66 SD), and 46.5 cm, respectively. He was immobile, uncommunicative, and had no visual tracking. His facial photographs at 3, 5, 10, and 15 years of age are shown in Figure 1D and Figure S4. He passed away after an anaphylactic shock reaction to egg white at 19 years of age.

Family 2

Two affected individuals were born to non-consanguineous Japanese parents. They were born without asphyxia after uneventful pregnancies. The first child (II-1; Individual 3) was born at 38 gestational weeks by cesarean section for breech presentation. Her birth weight, length and HC were 3112 g (−0.3 SD), 51.0 cm (+1.15 SD) and 34.5 cm (+1.17 SD). Her locomotive activity decreased during the month following birth. At 2 months old, she was taken to hospital because she did not cry or smile at others. A brain MRI at 3 months revealed a chronic subdural hematoma of the left brain and bilateral periventricular leukomalacia (Figure S3). A subsequent MRI at 7 months of age showed that the brain atrophy was progressive (Figure 3B). At 5 months, hypsarrhythmia detected by electroencephalogram (EEG) led to the diagnosis of West syndrome. Vitamin B6, nitrazepam, and zonisamide treatments were ineffective. At 6 months old, she was admitted to hospital for adrenocorticotropic hormone treatment, which was barely able to improve her voluntary movement, vocalization, and EEG findings (decreased frequency of seizures by more than half and a disappearance of hypsarrhythmia and suppression-burst patterns), but paroxysmal activity still remained. Head control, visual tracking and eye contact were absent. Her facial expression was impassive and her eyes were directed to the left. As she was unable to cry when hungry, breast milk was fed at fixed intervals. Her eyelash, corneal, and cough reflexes were normal. Her upper limbs were tonic and the DTR of her extremities was increased. Her muscle tone was deteriorating and her muscles were becoming small and soft. Because of respiratory failure, mechanical ventilation was started at 9 months of age, and a tracheotomy was performed at 18 months. Her motor developmental delay became more evident as time progressed. Facial photographs at 4 months and 1 year 10 months are shown in Figure 1D and Figure S4. At 2 years, she lost DTR and had tongue fasciculation, which may indicate the disease is affecting the lower motor neurons. At 4 years of age, brain CT indicated marked atrophy of the CNS with ventricular enlargement (Figure 3B and 3C). At the age of 11 months, MCV (right median nerve: 27 m/sec, left median nerve: 31 m/sec, normal range: 42.3±6.4 m/sec) was delayed and SCV (between the index finger and the wrist) (right median nerve: 34 m/sec, left median nerve: 36 m/sec, normal range: 32.6±6.4 m/sec) was normal, and visual evoked potential was undetectable. At least four episodes of elevated CK were noticed (285 IU/L at 7 months, 249 IU/L at 8 months, 199 IU/L at 13 months, and 182 IU/L at 3 years, normal range:

41–153 IU/L). These elevations may be explained by frequent tonic seizures. Currently, she is 10 years old and immobile.

The second child (II-2; Individual 4), a 7-year-old boy, was born at 39 weeks gestation by vaginal delivery. His birth weight, length, and HC were 3548 g (+1.36 SD), 51.5 cm (+1.2 SD) and 34.0 cm (+0.38 SD), respectively. He was hypotonic at 1 month of age. He was brought to hospital at 4 months with absent head movement, absent visual tracking and muscle weakness was noted. At 5 months of age, his locomotor activity, vocalization, and crying were weak and he made no eye contact. An ophthalmological examination revealed bilateral optic nerve atrophy, but no other fundus abnormalities. Routine laboratory tests were within normal ranges except for the slight elevation of serum aspartate aminotransferase (57 IU/L), alanine aminotransferase (65 IU/L), and CK (528 IU/L). After that, elevated CK was also observed at least three times: 752 IU/L at 11 months IU/L, 279 IU/L at 14 months, and 177 IU/L at 16 months. EEG showed multiple spikes in the occipital lobes (right > left). MCV (right median nerve: 20 m/sec, normal range: 37.0±4.4 m/sec, right ulnar nerve: 28 m/sec, normal range: 40.5±4.2 m/sec) was decreased and SCV (between the index finger and the elbow) (right median nerve: 42 m/sec, normal rage: 38.4±5.4 m/sec, right ulnar nerve: 44 m/sec, normal rage: 44.1±4.1 m/sec) was normal at 5 months of age. Brain MRI at 5 months and CT scans at 1 year and 6 months and 2 years showed progressive diffuse cerebral atrophy predominantly in the frontal lobe (enlargement of the subdural space and lateral ventricles and decreased volume of the white matter and prominent gyrus) and the brain stem (Figure 3D). Furthermore, brain MRI showed chronic subdural hematoma in the right lobe and cerebral atrophy mainly in the frontal lobe (Figure 3E). Low intensity of the pyramidal tract on T2-weight images suggested hypomyelination (Figure 3D). At 6 months, he suffered acute respiratory failure and was intubated and mechanically ventilated. One month later, a tracheotomy was performed. Facial photographs at 3 months, 7 months, and 1 year 5 months are shown in Figure 1D and Figure S4. A whole body CT at 6 months indicated remarkable muscle thinning and prominent fat tissues in the extremities, neck, chest, and pelvic area.

Family 3

Individual 5 (II-1) and 6 (II-2) were born to non-consanguineous Malaysian Chinese parents after an uneventful pregnancy. Individual 5 was born at term via caesarian section for meconium-stained amniotic fluid. His birth weight, length, and HC were 3400 g (50th centile) and 54 cm (90th centile) and 35 cm (50th centile). No obvious dysmorphic features were noted (Facial photographs at 1 and 2 years of age are shown in Figure 1D and Figure S4). Until 4 months of age, his development was almost normal regarding muscle tonus, cooing, and smiling in response to others, but after that his development was delayed and accompanied by poor head control and hypotonia. At 6 months of age, he had frequent and refractory generalized tonic seizures that were partially controlled by sodium valproate and clonazepam. A ketogenic diet started from 6 months of age was effective, but he showed progressive neuroregression. During his last examination at 2 years of age, he had severe microcephaly (HC 44 cm, −5 SD) and profound psychomotor retardation with generalized hypotonia, marked head lag, hyperreflexia, and positive plantar reflex. He was almost immobile and unable to roll over or grasp objects. He was unresponsive to his surroundings, not focusing or vocalizing. Funduscopy showed bilateral pale optic discs. EEG revealed multifocal epileptiform discharges. A brain MRI at 1.5 years of age showed hypoplasia of the corpus callosum, delayed myelination, and bilateral widened subarachnoid spaces (images unavailable). He had swallowing difficulties and passed away at 4 years of age due to severe pneumonia.

His younger sister (Individual 6), a 4-year-old girl, was born after 38 gestational weeks by emergency caesarian section for fetal distress, but without neonatal asphyxia. Her birth weight, length, and HC were 3.4 kg (50th centile) and 54 cm (90th centile) and 34 cm (25th centile), respectively. Like her brother she developed normally until 4 months old. Subsequently, she became floppy and achieved no further developmental milestones, including head control. At 12 months, intractable generalized tonic seizures were seen daily with subsequent neurological regression. Her first two seizures were provoked by fever. A ketogenic diet was started but did not achieve adequate ketosis, so was terminated. Only sodium valproate could partially control the seizures. On her last examination at 2 years 10 months of age, her weight, length, and HC were 10.6 kg (−1.5 SD), 87 cm (−1.2 SD), and 42.5 cm (−6 SD), respectively. Subtle dysmorphism was noted with a low anterior hairline, upslanted palpebral fissures and microcephaly (Figure 1D and Figure S4). She became immobile and unresponsive to her surroundings with generalized hypotonia, hyporeflexia, and marked head lag. Involuntary movement was not observed. An EEG at 1 year 4 months of age showed no epileptic discharge with normal background. A brain MRI at the same age indicated corpus callosum hypoplasia and generalized reduced white matter (Figure 3F).

Family 4

Individuals 7 (II-1) and 8 (II-2) were born to healthy first-degree cousins of Iraqi-Jewish ancestry. Individual 7 (II-1), an 18-year-old female, was born after an uneventful pregnancy. She started having febrile seizures at the age of 11 months. Later on, she developed absence seizures hundreds of times a day. Between 7−11 years of age, she was seizure-free. At 11 years, she was hospitalized for status epilepticus and intractable seizures. Currently, she has several types of seizures; complex partial, generalized tonic, and generalized tonic clonic seizures approximately twice a week. She has no myoclonic seizures. EEG revealed frequent spikes and irregular spike wave activity (about 3 per second) with frontal predominance, but no myoclonic patterns. Brain MRI at 1.5 years revealed delayed myelination (data not shown). Visual evoked potential and electromyogram were normal. Metabolic workup including amino acids, ammonia, lactic acid, biotinidase, very long chain fatty acid and carnitine was normal. Palmitoyl-protein thioesterase and tripeptidyl-peptidase I results for neuronal ceroid lipofuscinosis were also normal. Genetic tests for Angelman and velocardiofacial syndrome were negative. She was treated with valproic acid, clonazepam, ethosuximide, lamotrigine, clobazam, topiramate, and zonisamide with no response. She also failed to respond to a ketogenic diet. Currently she is treated with levetiracetam and clonazepam to control seizures. She has severe behavioral problems such as hyperactivity and agitation, which are treated with risperidone. She started to walk unassisted at 2 years and 4 months of age. Throughout her development, she only spoke a few words, and regression occurred after the onset of seizures (11 months of age). Her current weight, height, and HC are 50 kg, 160 cm, and 51.5 cm, respectively. She is able to communicate with family members using vocal sounds. She can walk and eat independently, but needs assistance dressing. She has no sphincter control and requires diapers. She frequently drools and is classified as having moderate intellectual disability. Neurological examinations show normal eye movements, normal muscle strength, but increased muscle tone and DTR with clonus and spread of reflexes and bilateral flexor plantar response. Cerebellar functions are normal.

Individual 8 (II-2), a 17-year-old female, started having seizures at the age of 9 months. Currently, she has two types of seizures: generalized tonic–clonic seizures twice a week, and absence seizures with eye blinking dozens of times a day, sometimes prolonged up to 20 minutes. She does not have myoclonic seizures. A brain MRI has not been performed. She was treated with valproic acid, carbamazepine, ethosuximide, lamotrigine, levetiracetam, and topiramate, but with no response. At present, she is treated with gabapentin and sulthiame, in addition to clonazepam during attacks. She has severe behavioral problems including hyperactivity and agitation (shouting and speaking loudly), which are treated with risperidone. She only speaks a few words, but can communicate with family members using vocal sounds. She can walk independently and is able to eat unassisted, but she needs help dressing. She has sphincter control. Her cognitive level has been defined as 'moderate intellectual disability'. Her current weight, height, and HC are 50 kg, 163 cm, and 51 cm, respectively. She has 2 café au-lait spots on her skin, one of which is very large (15 cm in size) on the leg. She has no dysmorphic features. A neurological examination revealed normal eye movements, normal cranial nerves, normal muscle strength and tone, increased DTR with clonus and spread of reflexes and bilateral flexor plantar response. Cerebellar functions are normal.

Supplementary Figures

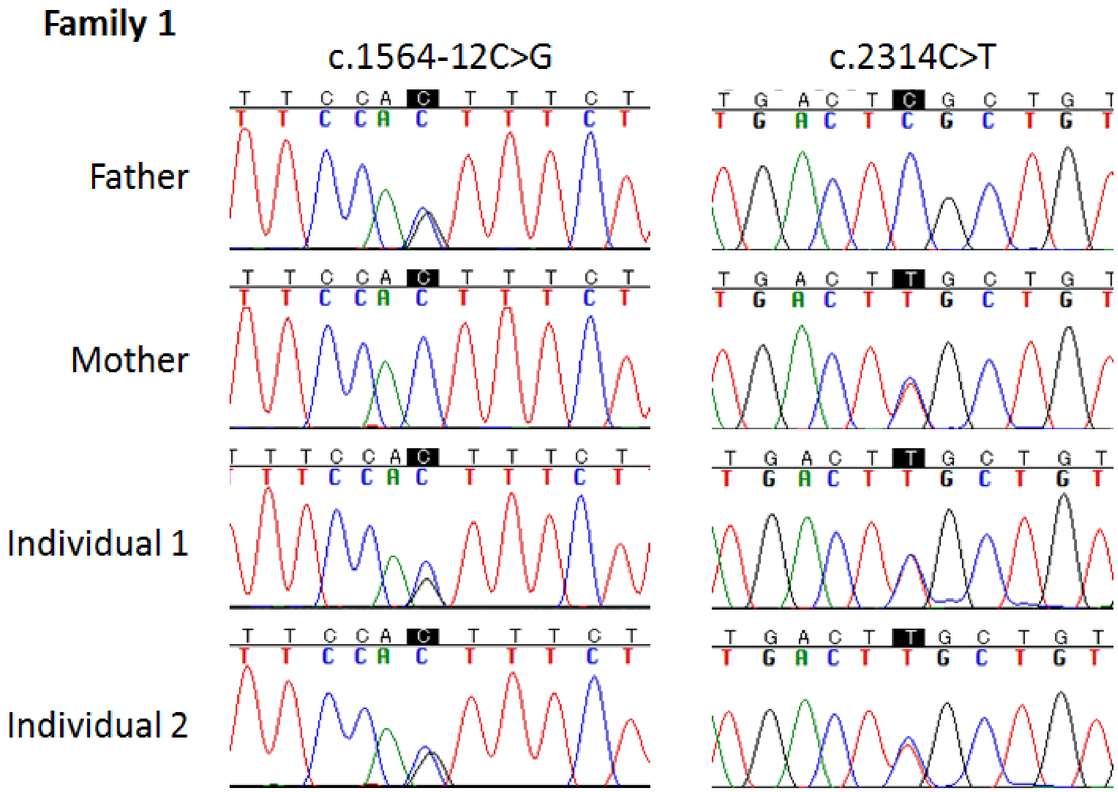

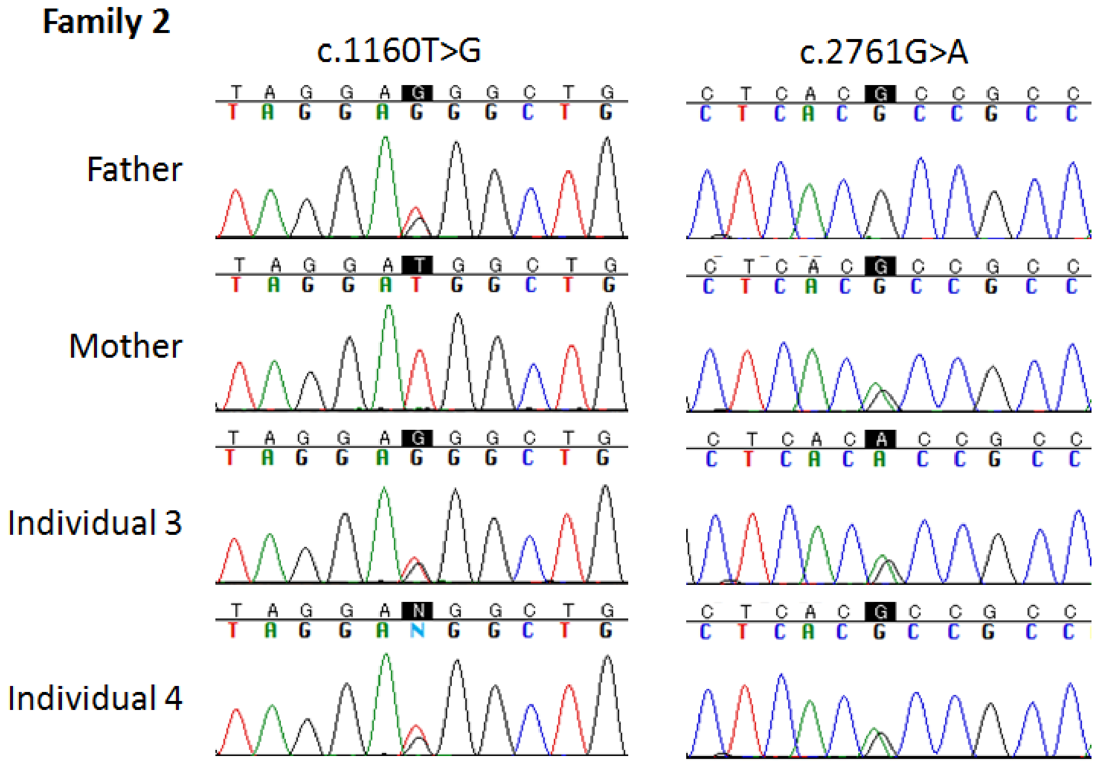

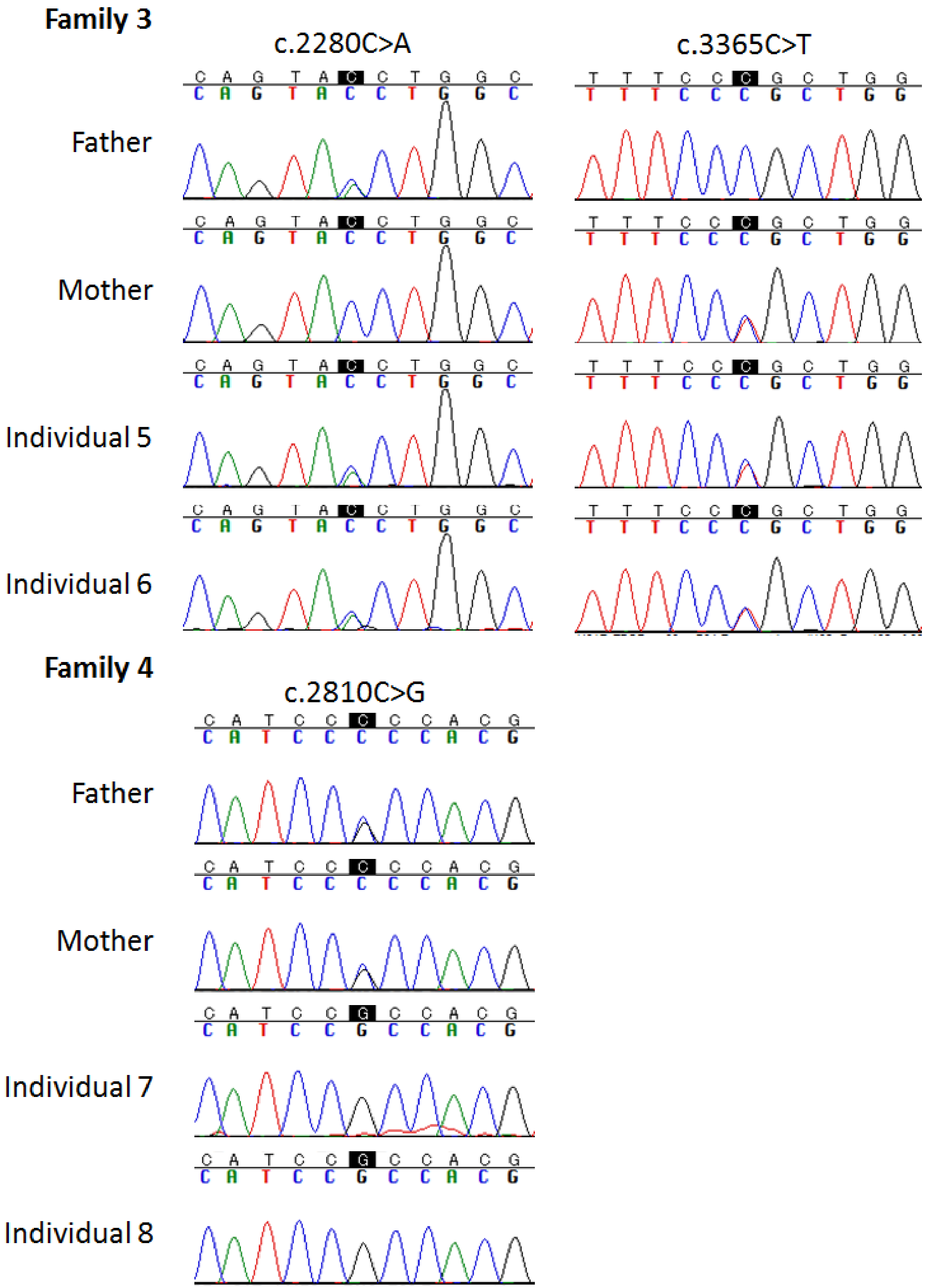

Figure S1. Electropherograms of *TBCD* Mutations Found in Families with Early-Onset Progressive Systemic Neurodegeneration

Affected individuals with biallelic *TBCD* mutations and their heterozygous carrier parents are clearly displayed with electropherograms.

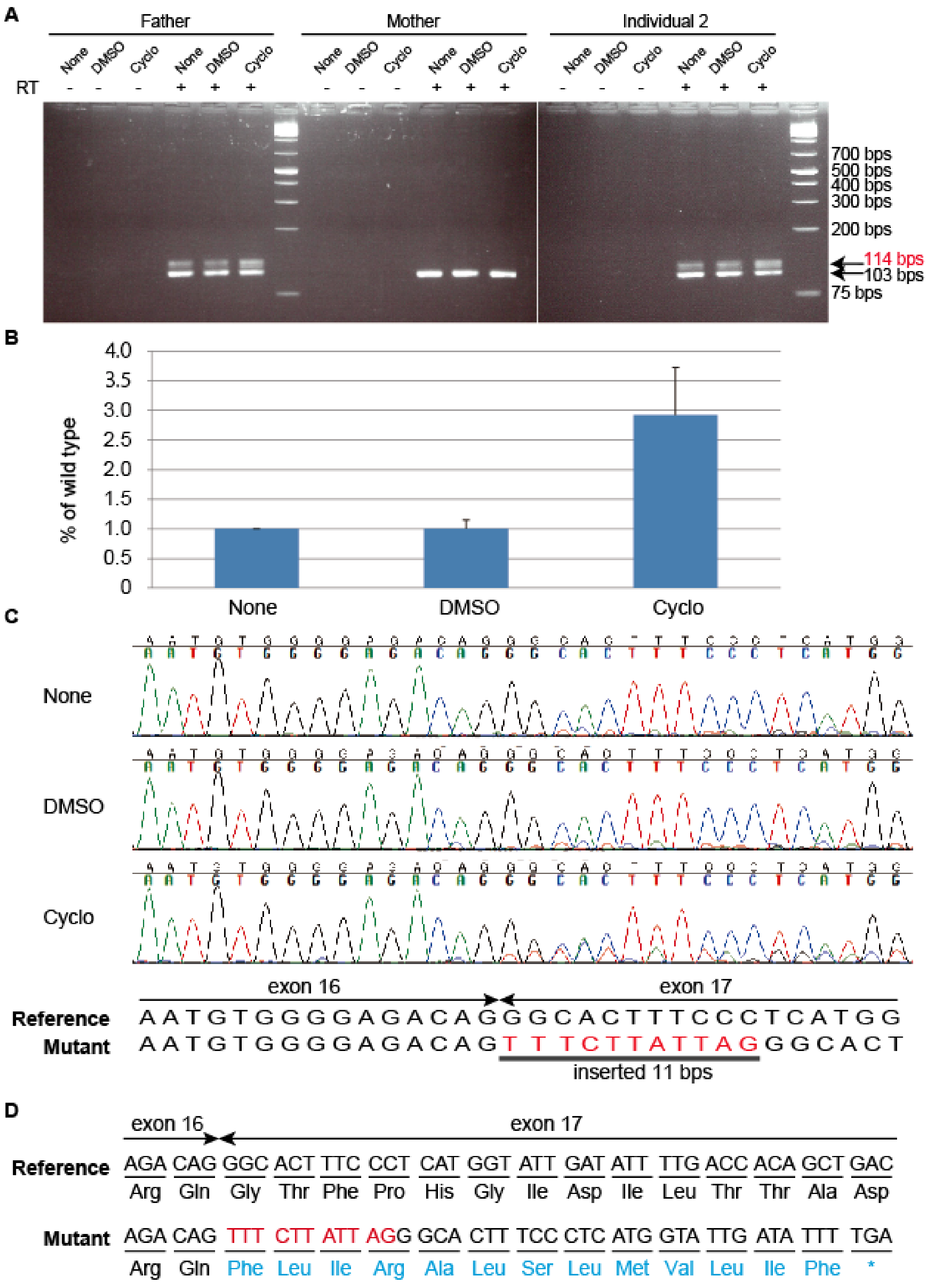

Figure S2. Aberrant Splicing Caused by c.1564-12C>G

(A) RT-PCR amplification of exon 15/16 to exon 17 using cDNA extracted from LCLs of Individual 2 and his parents using RNeasy Plus Mini Kit (Qiagen, Hilden, Germany) with/without cycloheximide to inhibit nonsense mediated decay. Total RNA was reverse-transcribed with SuperScript III First-Strand Synthesis System (Thermo Fisher, Scientific, Waltham, MA). The 103-bp product from normal allele and 114-bp aberrant product from mutant allele (c.1564-12C>G) are seen and were confirmed by Sanger method. The father and Individual 2 carrying this mutation showed the upper 114-bp product with stronger band intensity under the condition of cycloheximide. None: no treatment, DMSO: dimethyl sulfoxide, Cyclo: adding cycloheximide (Cyclo), –: with no reverse transcriptase, +: with reverse transcriptase. (B) Quantitative analysis of the aberrant band (114 bp) comparing the normal band (103 bp) under the condition of no treatment, adding solvent (control) or cycloheximide (n = 3). The gel images were captured by ChemiDoc Touch Imaging system (Bio-Rad Laboratories, Hercules, CA) and signal intensities were analyzed by Image Lab (Bio-Rad). The ratios of aberrant band to normal band were normalized to the condition of no treatment. The bar represents the standard error of the mean. (C) Electropherograms of RT-PCR products amplified from exon junction 13/14 to exon junction 18/19 (435 bps) using cDNA derived from Individual 2. Eleven nucleotides from intron 16 (in red) were aberrantly incorporated into cDNA in Individual 2 by abnormal splicing. Peak height of the abnormal allele was higher when cycloheximide interfered with nonsense mediated mRNA decay (NMD) compared with no treatment (None) or DMSO (solvent without cycloheximide). (D) Sequence of mutant cDNA and predicted protein caused by c.1564-12C>G. The inserted nucleotides are shown in red and altered amino acids are in light blue. This splice site mutation results in a frameshift (p.Gly522Phefs*14), but the truncated protein may not be present due to NMD. Primer sequences are available on request. The amplicon was sequenced on a 3130xl or 3500xL Genetic Analyzer (Applied Biosystems, Foster City, CA) and analyzed with Sequencher (Gene Codes, Ann Arbor, MI).

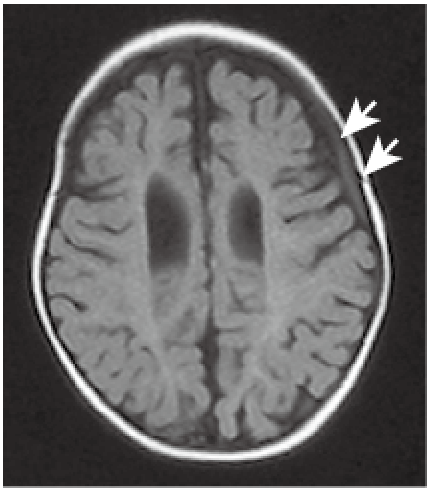

Figure S3. Brain Image of Individual 3

Brain MRI at 3 months indicated chronic subdural hematoma of the left brain (white arrows) and bilateral periventricular leukomalacia.

Figure S4. Facial Photographs of Affected Individuals with *TBCD* Mutations

Facial photographs of six affected individuals at different ages are shown.

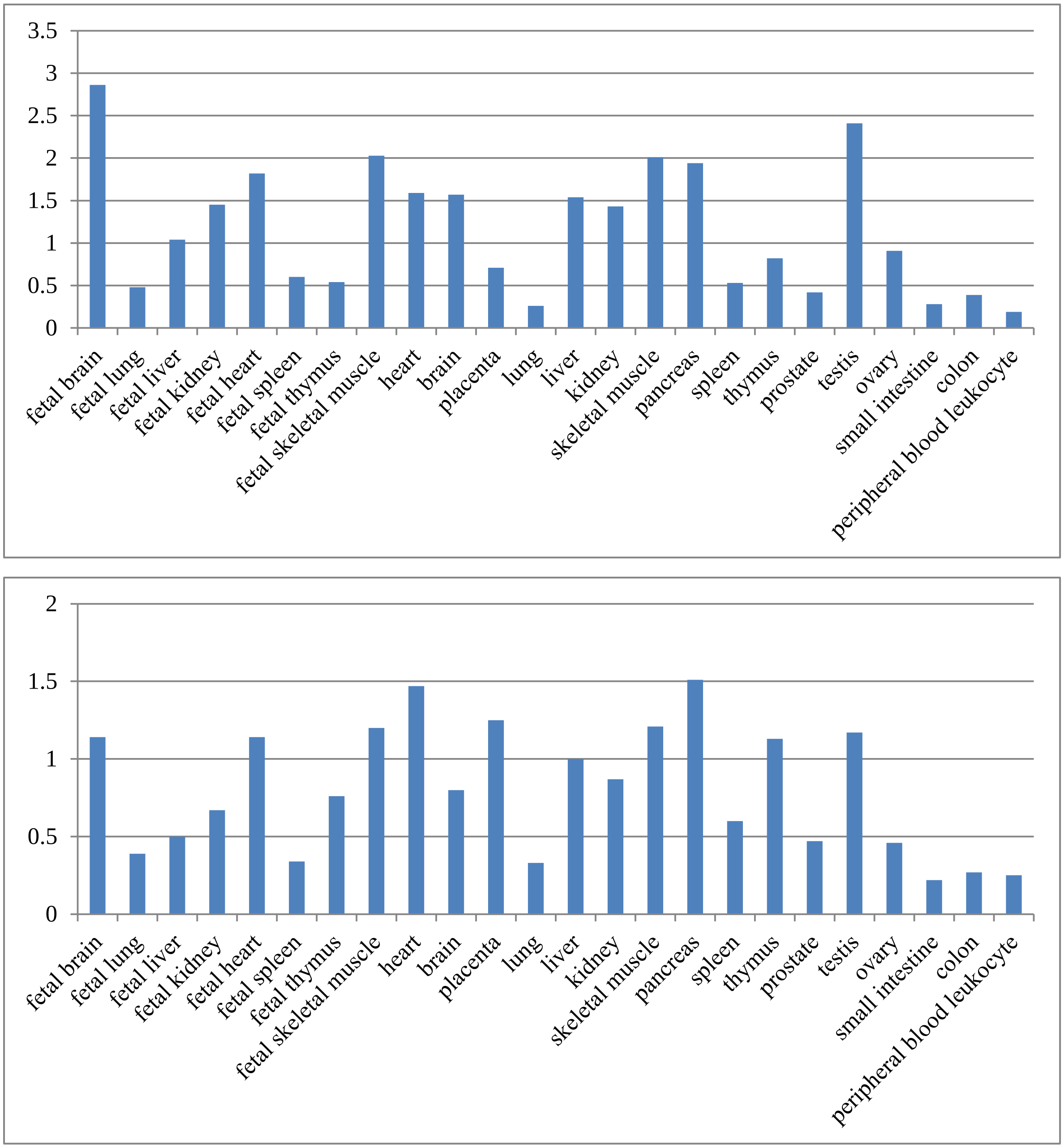

Figure S5. *TBCD* Expression in Human Tissues

Two independent experiments using two different probes (upper: Hs00195603_m1, lower: Hs00384759_m1) were performed after standardization to β-actin. cDNA from human fetal and adult tissues was purchased from Clontech (Mountain View, CA). Quantitative PCR was performed using a Rotor-Gene Q (Qiagen) and analyzed by the Delta Delta Ct method using Rotor-Gene 6000 Series software (Qiagen). The mean of two experiments are indicated. TBCD expression is abundant in brain, heart, skeletal muscle, and testis at fetal and adult stages.

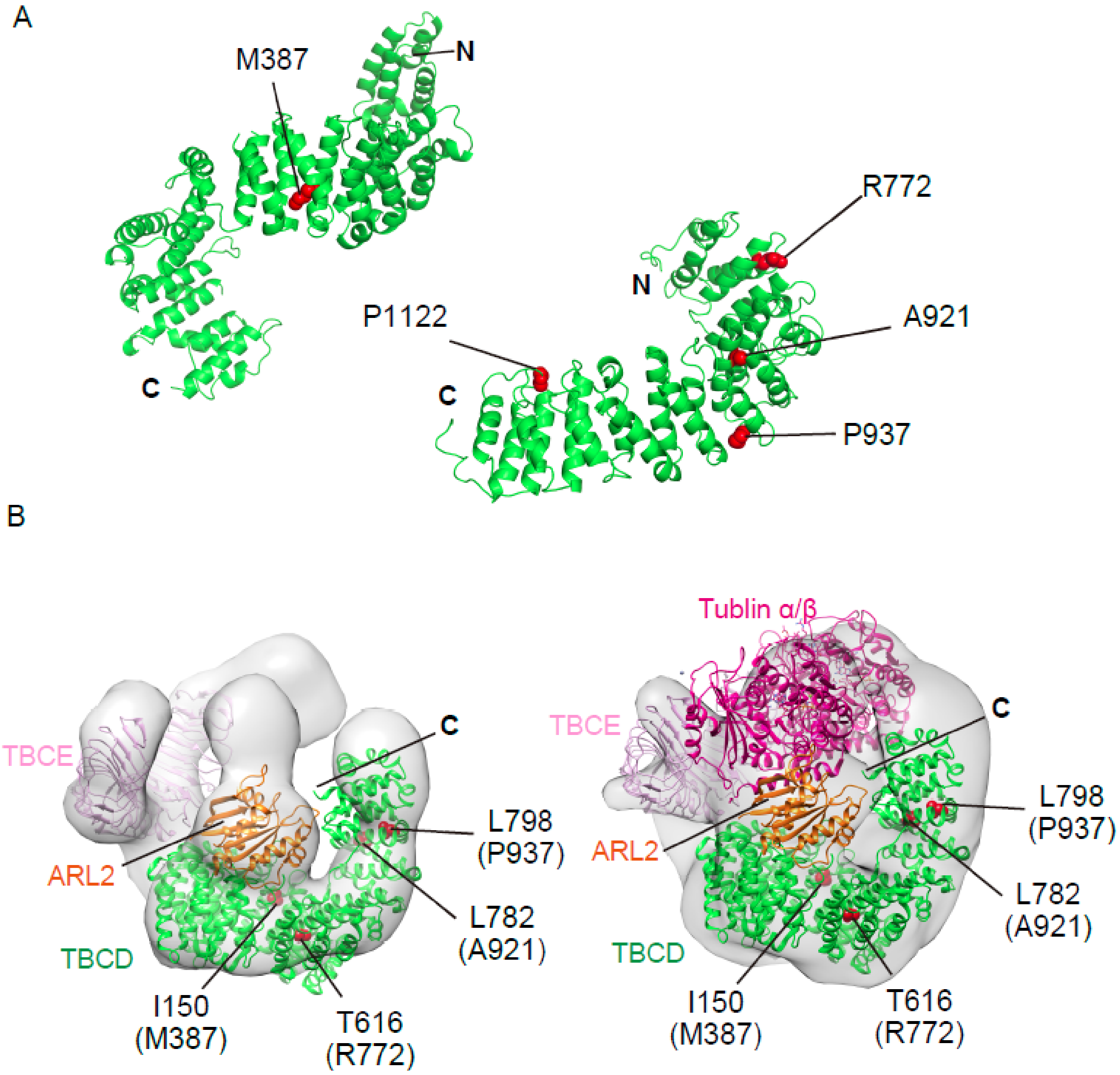

Figure S6. Mapping of the Mutation Sites onto Homology-Modeled Structures of TBCD

(A) The sites of the point mutations are shown in homology-modeled structures of two regions of TBCD, amino acid residues 20–695 (left) and 696–1192 (right). The residues at the mutation sites are shown as red van der Waals spheres. Annotations: N and C denote the N and C termini of the models, respectively. The models were constructed by the Phyre2 server[1] with each of the regions (amino acid residues 20–695 and 696–1192) as a query sequence. The crystal structure of karyopherin Kap121p (PDB code; 3W3Z)[2], which has a HEAT repeat, was selected as a structural template to build homology models of the two regions of TBCD. We verified the obtained alpha solenoid structure models using Alpha-rod Repeat Detector 2 (ARD2)[3] with the whole primary sequence of TBCD. (B) the EM-based pseudo-atomic models of core tubulin chaperones consisting of yeast TBCD, TBCE, and ARL2 with (right) or without (left) the yeast tubulin α/β dimer[4]. The residues at the mutation sites are shown as red van der Waals spheres. Amino acid numbers for yeast Cse1 are shown with those corresponding to human TBCD in parentheses. The pseudo-atomic models were constructed according to the previous report.[4] Briefly, we docked the atomic models corresponding to TBCD, TBCE, and ARL2 sequentially with or without a tubulin α/β dimer in this order into the EM maps, EMD-6390 or EMD-6392, respectively, using the 'fitmap' command in the UCSF Chimera software.[5] The following atomic models were used: the crystal structure of yeast nuclear export receptor Cse1 (PDB code 1Z3H)[6] for TBCD, the crystal structure of human ARL2 (PDB code 1KSJ)[7] for the ARL2 pillar region, and the electron crystallographic structure of α-β tubulin (PDB code 1JFF)[8] for the tubulin α/β dimer. For TBCE, we constructed a homology model using the 'intensive mode' of Phyre2 with the human TBCE amino acid sequence as a query. The mutation positions were mapped onto the Cse1 structure as follows. We searched homologous structures for human TBCD and yeast Cse1 using Phyre2 and identified the yeast karyopherin Kap121p structure (PDB code 3W3Z)[2] as a common homology model. We then mapped the mutation positions of human TBCD onto the yeast Kap121p structure, and subsequently onto the yeast Cse1 structure. The position of the P1122L mutation could not be determined because the C-terminal part of TBCE is missing from the modeled Cse1 structure. Note: The resolutions of currently available EM maps are too low to discuss the specific effects of the mutations on tubulin chaperone assembly.

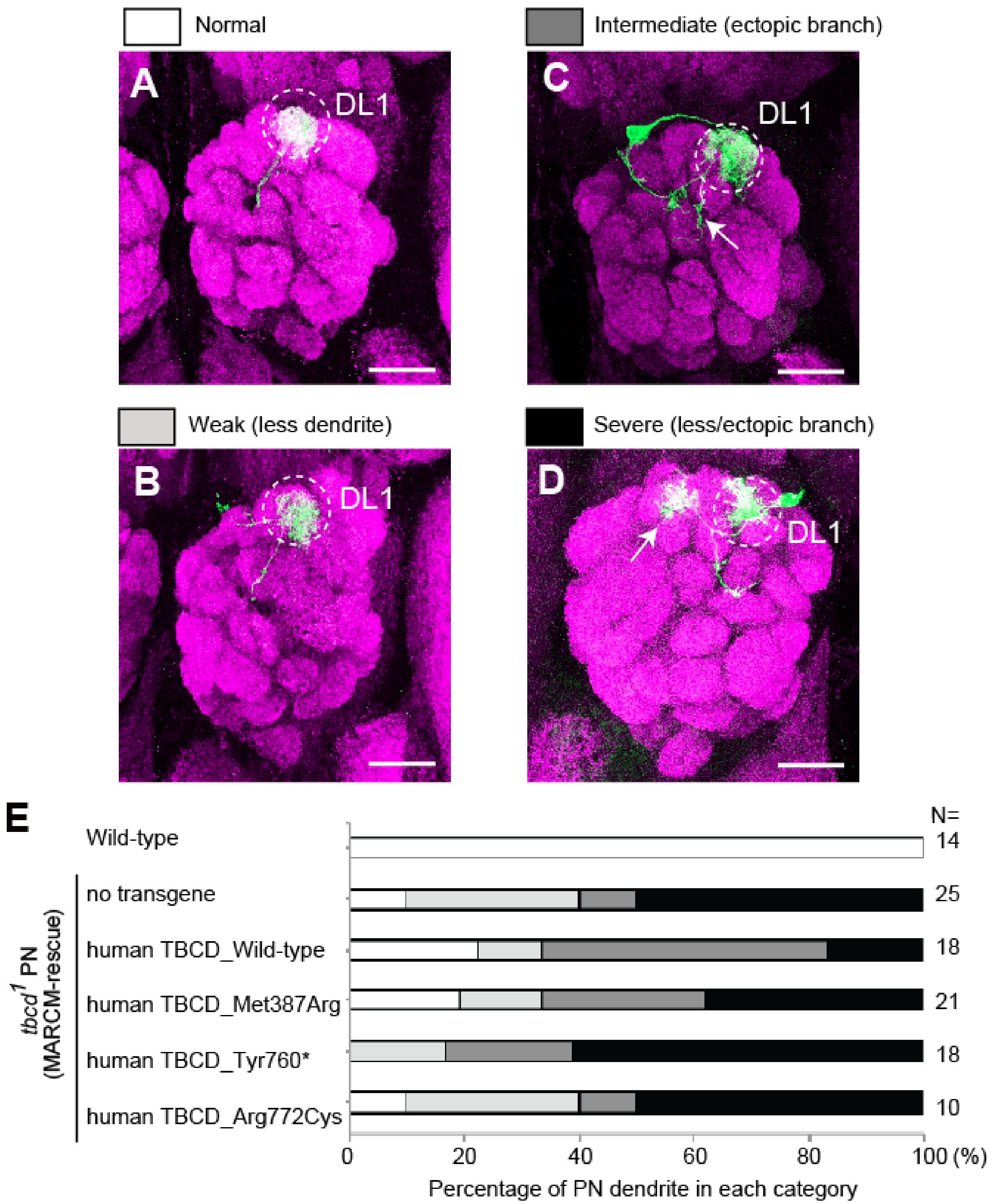

Figure S7. Effects of Mutations on Dendrite Morphology in *Drosophila Melanogaster* Olfactory Projection Neurons.

(A−D) Representative dendrite morphologies of *Drosophila* olfactory projection neurons. Dendrites of wild type DL1 single-cell clones (A) target the DL1 glomerulus. Dendrites of *tbcd*^{1} DL1 PN exhibited arborization and branching defects as shown in B–D. Arrows in C and D indicate ectopic dendritic branches. PN morphologies and Bruchpilot (presynaptic marker) are shown in green (anti-CD8 antibody) and magenta (nc82), respectively. Scale bars: 25µm. (E) Quantification of MARCM-rescue experiments. Each gray scale corresponds to a color in A–D above. N indicates the number of MARCM clones examined. Details for the generation of transgenic flies, MARCM clone induction, immunohistochemistry of fly brains, image processing and quantification methods are available upon request.

Table S1. Whole Exome Sequence Output and Coverage for Coding Sequences

Family ID	**Individual ID**	**Identification**	**Capture**	**Total (bps)**	**Mean depth**	**% ≥ 5×**	**% ≥ 10×**	**% ≥ 20×**
Family 1	I-1	Father	V5	3,199,010,619	95.57	97.2	96.2	93.1
Family 1	I-2	Mother	V5	2,902,625,566	86.72	97	95.8	92.2
Family 1	II-2	Affected individual	V5	3,766,100,939	112.51	97.3	96.4	93.7
Family 2	I-1	Father	V5	4,609,239,531	137.7	97.4	96.8	95.1
Family 2	I-2	Mother	V5	4,259,106,595	127.24	97.4	96.7	94.9
Family 2	II-1	Affected individual	V5	2,914,949,565	87.09	97	95.9	92.4
Family 3	II-1	Affected individual	V4	4,022,246,545	120.17	96.2	95.2	92.9
Family 4	II-1	Affected individual	V5	2,939,319,692	87.81	97.1	96	92.7

Table S2. Priority Scheme of Homozygous Variants in Four Families

	Family 1	**Family 2**	**Family 3**	**Family 4**
Homozygous in affected person as autosome*	2233	2219	2111	2094
Non-homozygous in father	378	400	NA	NA
Non-homozygous in mother	159	193	NA	NA
Frequency of ≤ 0.005 in ExAC	38	42	164	152
Frequency of ≤ 0.005 in EVS	35	39	141	136
Frequency of ≤ 0.005 in HGVD	22	25	114	118
Frequency of ≤ 5/575 in in-house database	3	4	1	33
Non-synonymous	3	3	1	25

NA: not analyzed by WES, ExAC: Exome Aggregation Consortium, EVS: Exome Variant Server, HGVD: Human Genetic Variation Database. *The number of the variants in exons and ± intronic 30 bp regions form exon–intron borders.

Table S3. Priority Scheme of Compound Heterozygous Variants in Four Families

	Family 1	**Family 2**	**Family 3**	**Family 4**
Heterozygous variants in affected person as autosome	4060	4073	3871	3676
Non-homozygous in father	3737	3719	NA	NA
Non-homozygous in mother	3412	3384	NA	NA
Frequency of ≤ 0.005 in ExAC	1727	1778	1828	1341
Frequency of ≤ 0.005 in EVS	1698	1748	1790	1254
Frequency of ≤ 0.005 in HGVD	1100	1101	1376	1210
Frequency of ≤ 5/575 in in-house database	578	534	889	918
Non-synonymous	421	401	664	667
Two or more variants in one gene	36	38	91	78
Compound heterozygous variant (gene)	14 (6)	19 (8)	ND	ND

NA: not analyzed by WES, ND: not determined, ExAC: Exome Aggregation Consortium, EVS: Exome Variant Server, HGVD: Human Genetic Variation Database.

Table S4. Clinical comparison between *TBCD* and *TBCE* mutations

	***TBCD* mutation** (number in our cohort)		***TBCE* mutation**[a]
Onset age	< 11 months		< 7 months
Intellectual disability	+	(8/8, 100%)	+
Microcephaly	+	(8/8, 100%)	+
Muscle weakness	+	(7/7, 100%)	Not mentioned
Regression	+	(6/6, 100%)	Not mentioned
Muscle atrophy	+	(6/8, 75%)	Not mentioned
Postnatal growth retardation	+	(6/8, 75%)	+
Seizure	+	(6/8, 75%)	-[b]
Respiratory failure	+	(5/8, 63%)	-
Optic nerve atrophy	+	(4/8, 50%)	Not mentioned
Bone abnormality	Bone fractures	(2/8, 25%)	Bone dysplasia [KCS]
Hypoparathyroidism	-		+
Recurrent infection	-		+ [KCS]
IUGR	-		+
Facial dysmorphism	-		+
Deep set eyes	-		+
Thin lips	-		+
Beaked nose tip	-		+
Depressed nasal bridge	-		+
External ear anomalies	-		+
Micrognathia	+		+
Brain MRI findings			
Hypoplastic corpus callosum	+		+
Decreased white matter	+		+

[a] The clinical information of *TBCE* mutation was based on papers by Sanjad et al. (1991) and Padidela et al. (2009).[9,10] [b] Only one affected individual showed seizures but with hypocalcemia.[10] [KCS]: The feature was only reported in Kenny-Caffey syndrome with *TBCE* mutations.

Table S5. Internal organ involvement in autopsied Individual 1

Organs	Findings
Heart	Normal shape. Normal cardiac muscle development.
Lung	Left: Lower lobe was atelectatic and shrunk.
	Right: Upper and middle lobes were atelectatic and shrunk.
Thymus	Prominent calcification was observed in Hassall’s corpuscles.
Thyroid	Not examined.
Parathyroid	Not examined.
Digestive tracts	No structural abnormality.
Liver	Fatty liver appearance.
Gallbladder	No remarkable change.
Adrenal grands	No remarkable change.
Spleen	No remarkable change.
Kidney	No remarkable change.
Urinary tracts	No remarkable change.
Urinary bladder	No remarkable change.
Uterus	No remarkable change.
Ovary	Multiple follicular cysts in both ovaries.

Table S6. Possible genotype–phenotype correlation between mutation and clinical severity

	Family 1		**Family 2**		**Family 3**		**Family 4**
Clinical severity	Profound		Severe		Severe		Mild
Mutation	c.1564-12C>G	c.2314C>T	c.1160T>G	c.2761G>A	c.2280C>A	c.3365C>T	c.2810C>G (homo)
Amino acid	p. Gly522Phefs*14	p.Arg772Cys	p.Met387Arg	p. Ala921Thr	p.Tyr760*	p.Pro1122Leu	p.Pro937Arg
Type	frameshift	missense	missense	missense	nonsense	missense	missense
Binding with ARL2	NA	↓	↓↓	↓	↓	↓	→
Binding with TBCE	NA	↓	↓↓	↓↓	↓↓	↓↓	↓
Binding with β-tubulin	NA	↓↓	↓↓	↓↓	↓↓	↓↓	↓

NA: not assessed as TBCD protein may not exist due to NMD.

Supplemental References

1. Kelley, L.A., Mezulis, S., Yates, C.M., Wass, M.N., Sternberg, M.J. (2015). The Phyre2 web portal for protein modeling, prediction and analysis. Nat Protoc 10, 845-858.

2. Kobayashi, J., Matsuura, Y. (2013). Structural basis for cell-cycle-dependent nuclear import mediated by the karyopherin Kap121p. J Mol Biol 425, 1852-1868.

3. Fournier, D., Palidwor, G.A., Shcherbinin, S., Szengel, A., Schaefer, M.H., Perez-Iratxeta, C., Andrade-Navarro, M.A. (2013). Functional and genomic analyses of alpha-solenoid proteins. PLoS One 8, e79894.

4. Nithianantham, S., Le, S., Seto, E., Jia, W., Leary, J., Corbett, K.D., Moore, J.K., Al-Bassam, J. (2015). Tubulin cofactors and Arl2 are cage-like chaperones that regulate the soluble alphabeta-tubulin pool for microtubule dynamics. Elife 4.

5. Pettersen, E.F., Goddard, T.D., Huang, C.C., Couch, G.S., Greenblatt, D.M., Meng, E.C., Ferrin, T.E. (2004). UCSF Chimera--a visualization system for exploratory research and analysis. J Comput Chem 25, 1605-1612.

6. Cook, A., Fernandez, E., Lindner, D., Ebert, J., Schlenstedt, G., Conti, E. (2005). The structure of the nuclear export receptor Cse1 in its cytosolic state reveals a closed conformation incompatible with cargo binding. Mol Cell 18, 355-367.

7. Hanzal-Bayer, M., Renault, L., Roversi, P., Wittinghofer, A., Hillig, R.C. (2002). The complex of Arl2-GTP and PDE delta: from structure to function. EMBO J 21, 2095-2106.

8. Lowe, J., Li, H., Downing, K.H., Nogales, E. (2001). Refined structure of alpha beta-tubulin at 3.5 A resolution. J Mol Biol 313, 1045-1057.

9. Sanjad, S.A., Sakati, N.A., Abu-Osba, Y.K., Kaddoura, R., Milner, R.D. (1991). A new syndrome of congenital hypoparathyroidism, severe growth failure, and dysmorphic features. Arch Dis Child 66, 193-196.

10. Padidela, R., Kelberman, D., Press, M., Al-Khawari, M., Hindmarsh, P.C., Dattani, M.T. (2009). Mutation in the TBCE gene is associated with hypoparathyroidism-retardation-dysmorphism syndrome featuring pituitary hormone deficiencies and hypoplasia of the anterior pituitary and the corpus callosum. J Clin Endocrinol Metab 94, 2686-2691.